A&A, 713, A103 (2026)
https://doi.org/10.1051/0004-6361/202659612

Astronomy & Astrophysics

MUSE imaging spectroscopy of the fullerene planetary nebula Tc 1

J. R. Walsh[1,⋆], M. J. Barlow[2], A. Monreal-Ibero[3], J. Cami[4,5], E. Peeters[4,5], R. Wesson[6], J. Bernard-Salas[7], N. L. J. Cox[7], and G. F. J. Watt[4]

[1] European Southern Observatory, Karl-Schwarzschild Strasse 2, 85748 Garching, Germany
[2] Department of Physics and Astronomy, University College London, Gower Street, London WC1E 6BT, UK
[3] Leiden Observatory, Leiden University, PO Box 9513, 2300 RA Leiden, The Netherlands
[4] Department of Physics and Astronomy, The University of Western Ontario, London ON N6A 3K7, Canada
[5] Institute for Earth and Space Exploration, The University of Western Ontario, London, ON N6A 3K7, Canada
[6] Cardiff Hub for Astrophysics Research and Technology (CHART), School of Physics and Astronomy, Cardiff University, The Parade, Cardiff CF24 3AA, UK
[7] ACRI-ST, Centre d'Etudes et de Recherche de Grasse (CERGA), 10 Av. Nicolas Copernic, 06130 Grasse, France

Received 26 February 2026 / Accepted 18 June 2026

ABSTRACT

Aims. The planetary nebula Tc 1 (PN G345.2−08.8), one of the rare group of Galactic PNe showing fullerene emission in the infrared, is spatially extended with high a surface brightness. Optical imaging spectroscopy enables the line and continuum structure and diagnostics to be examined, and permits a search for any correlations to the presence of fullerene dust.

Methods. Tc 1 was observed with MUSE wide field mode with adaptive optics, wavelength range 4700–9300 Å, at three exposure levels to ensure unsaturated emission lines. Extinction, electron temperature (T_e), and density (N_e) diagnostic images are presented from collisionally excited and recombination line ratios.

Results. The nebula has a high surface brightness core, with a diameter 12″, an elliptical ring of major axis 2.8″ around the central star and some low ionization knots, and an extended halo of 55″ in diameter; between the core and halo is an annulus with intermediate properties, including a higher T_e and a lower N_e than in the core. The spectrum of the central star was extracted and fitted by a 31 000 K model atmosphere and is of type O7.5I(f). The image of optical extinction from H Balmer line ratios is highly structured, and shows an annulus, which is adjacent to the core, of low extinction, with values lower than the line-of-sight interstellar extinction. Instrumental effects to account for this anomalously low extinction area were investigated and intrinsic effects from the scattering properties of the nebular dust; neither can entirely explain the low-extinction region and the most likely cause is a local non-standard dust reddening law. This low extinction region additionally shows an anomalously high He i 7281/6678 Å line ratio, possibly caused by a contaminating line, but none have been conclusively identified; its origin remains unresolved. Spectra over extended regions were also analysed and distinct enhancement of the continuum above the expected nebular continuum (as also seen in some other PNe observed with MUSE) was found.

Conclusions. The annulus of low extinction occurs outside the region of strongest fullerene emission, in the zone where N_e declines and T_e rises. A change in dust properties linked to conditions in this transition region between the higher density core nebula and lower density halo is deduced.

Key words. planetary nebulae: general – planetary nebulae: individual: Tc 1

1. Introduction

Tc 1 (Thackeray 1950), whose alternative name is IC 1266 (PN G345.2−08.8), is an apparently normal low ionization planetary nebula (PN), but it was the first PN to have fullerene emission (C_{60}) detected in the mid-infrared (Cami et al. 2010). The number of such planetary nebulae (PNe) with fullerene emission is still low (25 – García-Hernández et al. (2012), Otsuka (2019) in the Galaxy, Large Magellanic Cloud (LMC), and Small Magellanic Cloud (SMC)). Fullerenes are now detected in many other interstellar environments, such as post-asymptotic giant branch (AGB) circumbinary disks (Gielen et al. 2011), the Orion Nebula (Rubin et al. 2011), reflection nebulae (Sellgren et al. 2010) and even the diffuse interstellar medium (Berné et al. 2017).

Tc1 has a high surface brightness core ∼12″ in diameter surrounded by a much fainter halo extending to radii ∼25″ (Schwarz et al. 1992; Corradi et al. 2003). It is a low ionization PN: the highest ionization species observed is [O iii] (ionization energy 35.1–54.9 eV), and it is classified as C-rich (log(C/O) of +0.14) on the basis of optical (Williams et al. 2008) and ultra-violet (International Ultra-violet Explorer, IUE) spectra (Pottasch et al. 2011). The central star (CD −46° 11 816) is bright (Gaia G mag. = 11.269) with a parallax of 0.2672 ± 0.0344 mas, a Galactic plane object in the direction to the Galactic bulge; Chornay & Walton (2021) derived a distance of 3530 $^{+380}_{-329}$ pc.

Aleman et al. (2019) presented some deep spectroscopy of Tc 1 with the European Southern Observatory (ESO) Very Large Telescope (VLT) X-shooter instrument (Vernet et al. 2011) for a slit offset from the nebula central star (CSt) over the bright core. The X-shooter slit (length 11″) sampled the bright core, but not the halo. Near ultra-violet, blue, and red spectra were presented (wavelength coverage 3250–5550 and 5660–10 050 Å) and the

⋆ Corresponding author: jwalsh@eso.org

Table 1. Log of MUSE observations of Tc 1.

Target	RA (h m s)	Dec (° ′ ″)	T exp (s)	PA (°)	Date	Dataset UT(h:m:s)	Airmass	DIMM (″)
Tc 1	17 45 35.44	–46 05 26.3	40.0	0	2022-06-29	02:29:41.267	1.134	0.56
Tc 1	17 45 35.44	–46 05 26.3	40.0	0	2022-06-29	02:31:35.649	1.131	0.51
Tc 1	17 45 35.44	–46 05 26.3	40.0	0	2022-06-29	02:33:29.903	1.129	0.44
Tc 1	17 45 35.50	–46 05 26.3	40.0	0	2022-06-29	02:36:02.866	1.125	0.53
Tc 1	17 45 35.50	–46 05 26.3	40.0	0	2022-06-29	02:37:57.262	1.123	0.57
Tc 1	17 45 35.50	–46 05 26.3	40.0	0	2022-06-29	02:39:51.465	1.121	0.57
Tc 1	17 45 35.50	-46 05 25.7	40.0	0	2022-06-29	02:42:23.818	1.118	0.44
Tc 1	17 45 35.50	–46:05:25.7	40.0	0	2022-06-29	02:44:18.371	1.116	0.50
Tc 1	17 45 35.50	–46 05 25.7	40.0	0	2022-06-29	02:46:12.929	1.113	0.55
Tc 1	17 45 35.44	–46 05 25.7	40.0	0	2022-06-29	02:48:45.497	1.111	0.45

Notes. The column labelled DIMM lists the value of the VLT Differential Image Motion Monitor image quality ('seeing') for the observation. Only the first ten entries of this table are shown; the full table is available in electronic form at the CDS.

emission lines were analysed for extinction, physical diagnostics – electron temperature (T_e) and volume electron density (N_e, cm^{-3}), and ionic and total abundances. The total abundances derived from a photoionization model were log(He/H) = –0.098 and for O, log(O/H) = −3.60 from the collisionally excited lines (CELs) and −3.06 from the optical recombination lines (ORLs); with CELs log(N/O) = −1.00 (Aleman et al. (2019), their Table 4). From the photoionization model, the CSt was matched by a 30 000 or 32 000 K black body; using the Gaia distance, the luminosity is then 8200 or 9000 $L_\odot$.

Given the deep spectroscopic study conducted by Aleman et al. (2019), although with only a single short slit, the next step in optical observations of Tc 1 is integral field spectroscopy (IFS). Apart from the central star's low effective temperature and high nebular C/O ratio, the X-shooter spectroscopy did not reveal any particular aspect of the nebula to indicate that it was otherwise exceptional relative to the more common fullerene non-detected PNe. Using the large field Multi Unit Spectroscopic Explorer (MUSE) IFS on the VLT (Bacon et al. 2010), with a field that covers the core and the complete halo in a single pointing, we have investigated in depth possible spectro-spatial features that might betray the role of fullerenes in the optical structure and properties of Tc 1.

The outline of the paper is as follows: Section 2 presents the MUSE observations and a brief description of the reduction of instrument signature. This is followed by a presentation of the emission line imaging results in Section 3, including correction for the effect of field stars on the images over the area of the MUSE field and a combination of images from the three exposure times. Section 4 presents the derived diagnostics:- extinction from Balmer line ratios and physical conditions T_e and N_e from the CEL and ORL ratios. Section 5 presents a wide ranging discussion on the emission line morphology, the complex extinction structure and a possible model to explain the area of anomalously low extinction, the parameters of the CSt as extracted from the MUSE cube, summed spectra for selected spatial areas of Tc 1, and finally the role of critical further observations, particularly in the infrared. The papers ends with Conclusions. Four appendices consider the following: the correction procedure of field star spectra; the application of image restoration to investigate the reality of the sharp changes in areal extinction; a dust scattering model to try to explain these features; and a comparison of a residual continuum signal in the summed spectra of several PNe observed with MUSE, which was not explained by nebular and stellar contributions. A fifth appendix tabulates the summed fluxes for the emission lines in the three spatial areas and the total imaged area for Tc 1.

2. Observations and data reduction

Tc 1 was observed in service mode in 2022 in dark time with MUSE (Bacon et al. 2014) in wide field (59.9×60″) mode (WFM) with adaptive optics (AO) correction fed by the Adaptive Optics Facility (AOF) instrument GALACSI in ground layer AO (GLAO) mode (Stuik et al. 2006; Ströbele et al. 2012). The MUSE nominal wavelength coverage (4700–9300 Å) was chosen (however, on account of the contamination in the region of the Na I D lines at 5890.0, 5895.9 Å from the AOF laser guide stars, a blocking filter masks the spectral range 5806–5965 Å). The mean (2 pixel) spectral resolving power of MUSE is ≃2800.

Three exposure times were specified: the shortest 40 s to ensure all, including the strongest emission lines (Hα, [O III] 5007 Å), were detected unsaturated; 101 s for lines of intermediate strength to be unsaturated; and 595 s for detection of faint lines (e.g. ≪1% of Hβ). The range of exposure times was chosen so that the fluxes of the faintest and strongest lines over a range of >100 could be compared. The total exposure time was 4.29 hours divided between 48 40 s exposures (0.53 h), 16 101 s exposures (0.45 h) and 20 of 595 s (3.31 h), taken over four nights in VLT service mode. 90° rotations (PAs of 0 and 90 °) and dithers of 0.4″ offsets were applied in order to help mitigate the pattern of the 24 individual integral field units of MUSE. Since the full extent of Tc 1, known from previous studies, did not fill the MUSE field of view, the background sky could be estimated from the edges of the field. Table 1 provides a log of these observations. Column 8 lists the mean airmass per exposure and column 9 the differential image motion monitor (DIMM) image quality. On 2022-06-16 four 595 s exposures were obtained, but the seeing was poor (>1.20″) and these data were excluded from the final combination of the longest exposure set.

The MUSE WFM-AO-N observations of Tc 1 were reduced with *EsoRex* (version 3.13) scripts and the MUSE instrument pipeline, version 2.8.7 (Weilbacher et al. 2014, 2020). Compatible master bias, master flat, master dark, wavelength calibration table (WAVECAL), trace table, twilight cube (for sky flat correction), and spectrophotometric response (STD_RESPONSE), all local in time to the observations, were downloaded from the

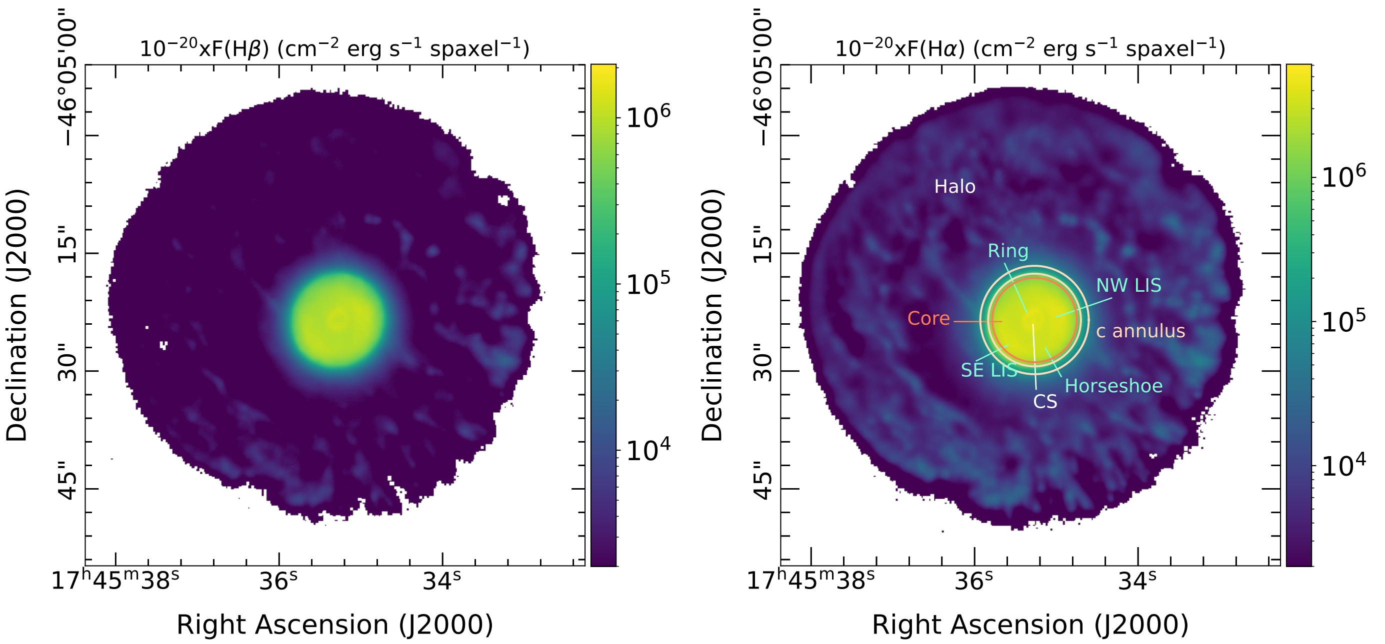

Fig. 1. Morphology of Tc 1 in H Balmer emission. Left: log flux (erg cm^{-2} s^{-1}) of Hβ extracted from the 40 s cube, displaying the bright core and low surface brightness halo to 3σ line flux detection per 0.2×0.2″ spaxel; Right: composite image of Tc 1, composed of the bright core in Hα (linear stretch) and the fainter surroundings and halo in [N II] 6583 Å (log stretch), with the morphological features of the nebula indicated. All images are oriented: E left, N up.

ESO MUSE calibration database[1]. The spectral trace table from the calibration database dated from 2021 and the Paranal atmospheric extinction table was from 2014. The spectrophotometric standard star used to establish the flux calibration was GD 153 (Moehler et al. 2014).

The correction for the presence of Raman scattered lines, induced by the AOF Na laser guide stars (Vogt et al. 2017), was made as included in the MUSE *sci_basic* task. Using exposures in a V'-band filter (square profile, 5350–5650 Å) and centroiding (IRAF[2] *imexam*) the bright CSt, the offsets between exposures were determined and used in precisely aligning the individual exposures to produce a single combined data cube for each exposure level.

The resultant sky-subtracted cubes have dimensions 318 (α) by 319 (δ) [63.6 × 63.8″ with 0.2″ spaxels] by 3681 (λ) voxels (4700–9300 Å) at the default binning of 1.25 Å. Extracting the same V' filter images from the final cubes and measuring a set of (17) well separated and apparently single stars, the mean and standard deviation of the full width at half maximum (FWHM) Gaussian image quality was measured as: 0.579 ± 0.023 ″ for the 40 s exposure; for the 101 s set, 0.602 ± 0.027″; and 0.645 ± 0.021″ for 595 s exposure. The absolute astrometry was adjusted using the coordinates of the CSt from the *Gaia* DR3 catalogue (Lindegren et al. 2021): (Gaia DR3 5954912374289120896, α, δ 17^{h} 45^{m} 35.28^{s}, −46° 05′ 23.87″) for the 40 s exposure where the V' stellar image was unsaturated.

3. Results: Imaging

The emission lines in each combined cube for the three exposure levels were analysed with a semi-automatic Gaussian line fitting task, described in Walsh et al. (2018). This task fits lines using a pre-defined list of emission lines expected in the spectrum and the list was produced from the Tc 1 line list in Aleman et al. (2019). If a line from this list was not detected to a given σ above the background in the MUSE spectrum, no Gaussian fit was performed. The Gaussian fitted lines in each spaxel were converted into emission line flux and error images (and line wavelength and width images were also recorded); the Gaussian fit errors were propagated from the MUSE variance cube.

Figure 1 shows the appearance of Tc 1 in H recombination lines and Figure 2 for CELs of varying ionization. Hβ illustrates the general features of the nebula morphology (Figure 1, left). The outer cut-off in Hβ flux is at 3σ detection per spaxel (0.04″^{2}). A composite image of Tc 1, composed of the bright core in Hα (linear stretch) and the fainter surroundings and halo in [N II] 6583 Å (log stretch), both extracted from the 40s cube, is shown in Figure 1, right. The main features of the nebula, which are subsequently discussed (see Sect. 5.1), are indicated. The two regions of low ionization systems (LIS), analysed by Bouvis et al. (2025), are also labelled. The half mean surface brightness extent of the core (radius = 5.4″) is indicated in orange and the annulus of lower extinction values (‘c annulus’, see Sects. 4.1 and 5.2) between radii 5.9″ and 6.9″ is indicated in pink.

The highest ionization energy emission detected, that of [O III] 5007 Å, is shown in Figure 2, upper left; intermediate O ionization [O II] (sum of 7320+7330 Å line images) is shown at

[1] When applying the calibration database reference files, bright and dark rows were found on extracted images from the final data cubes from several nights of observation, irrespective of exposure time. This problem was tracked down to the database slit illumination files used (tagged ILLUM in the MUSE pipeline), which produced slightly shifted tracing of the IFU slits from those recorded each night. When applying the correct daily illumination files to the basic calibration steps, the alternate brighter and darker rows were found to disappear.

[2] IRAF is distributed by the National Optical Astronomy Observatories, which are operated by the Association of Universities for Research in Astronomy, Inc., under cooperative agreement with the National Science Foundation.

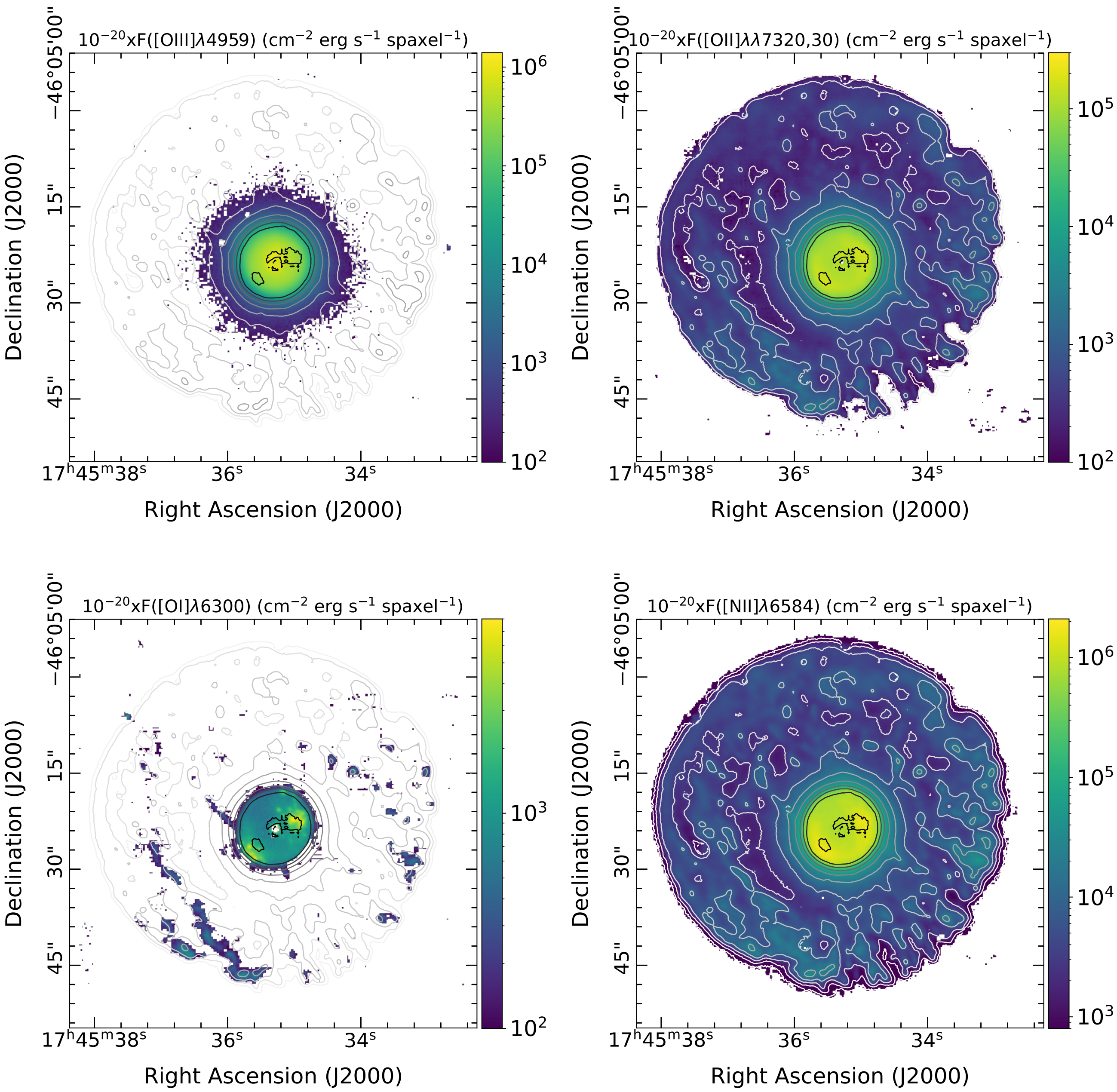

Fig. 2. Morphology of Tc 1 in some CELs. Upper left: log flux (erg cm^{-2} s^{-1}) of [O III] 5007 Å, extracted for the 40 s cube, displaying the bright, rather featureless core and low surface brightness diffuse halo; Upper right: log flux (erg cm^{-2} s^{-1}) of [O II] 7320+7330 Å, from the 40 s cube, exhibiting the contrasting low ionization compact features in the core and the halo; Lower left: linear flux (erg cm^{-2} s^{-1}) of [O I] 6300 Å line emission from the 595 s cube emphasising the compact knots over the core and filaments in the halo; Lower right: linear flux (erg cm^{-2} s^{-1}) of [N II] 6583 Å, again from the 40 s cube, showing the contrasting appearance of the core and halo with respect to lines of O. The Hβ line contour map is superposed on the collisionally excited line images and all images are displayed to a cutoff of 3σ line flux per spaxel.

upper right and the neutral oxygen emission [O I] (lower left). The contrasting morphology in the strongest low ionization line [N II] 6583 Å is shown at lower right. The striking difference between the appearance in high and lower ionization images is the strength and structure of the outer extent of the nebula, which is beyond the bright core, subsequently referred to as the halo. The presence of a halo can be deduced from the image in Corradi et al. (2003), their Fig. 16, but its detailed structure is now revealed for the first time. While there is diffuse emission in [O III] outside the bright core, it is very faint and lacks the structure seen in lower ionization ([O II] and [N II]). The [O III] emission surface brightness in the halo is on average 19 times fainter than for [N II] for the same (14″) radial offset. In [O I], the morphology emphasises compact knots both within the core (including the LIS) and in the halo.

3.1. Effect of field stars

Before accurate emission line maps can be analysed, the problems posed by the presence of the many field stars requires

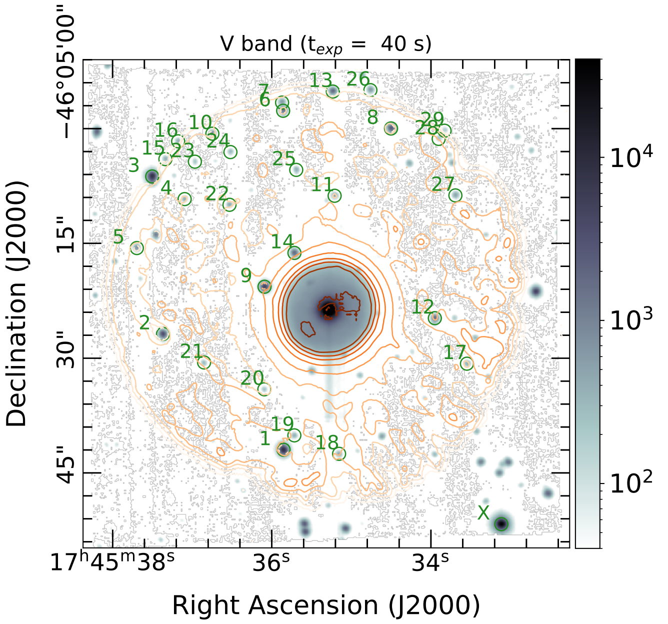

Fig. 3. v' band (5400–5600 Å) image in a linear flux scaling (from the 40 s exposure cube) showing the stars in and around Tc 1. The stars whose spectra were matched to correct for the presence of underlying Hβ and Hα over the halo are numbered (see text for details). Star X is the next brightest star after the CSt and occurs outside the halo; it was used as a point spread function (see Appendix B). The contour map was derived from the Hβ image (Fig. 1 upper left).

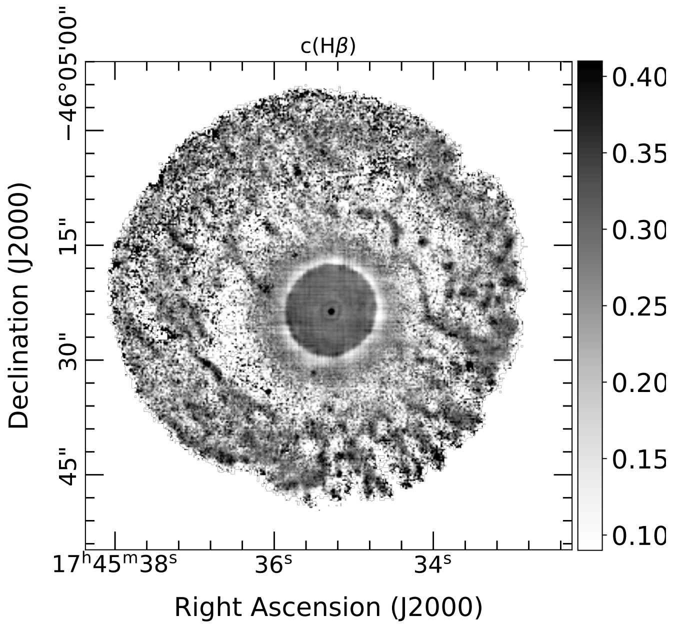

Fig. 4. Image of the Tc1 extinction, log c(Hβ), from Hα/Hβ compared to the Case B value combining the ratios from the 40 s, 101 s, and 595 s cubes. See text for more details.

consideration. Over the halo where the emission surface brightness is much lower than in the core, an emission line fitted on a late type stellar continuum spectrum can lead to misestimation of line fluxes, particularly for Balmer lines, since the Gaussian line task only fits a low order spline to the continuum adjacent to emission lines. The narrow v' (5400–5600 Å) continuum image, which is shown in Figure 3, demonstrates the scope of the problem: a poorly fitted emission line in the halo can be mistaken for an emission line knot, of which a few are coincident or close to field stars; an erroneous extinction estimate from the Hα/Hβ ratio at the position of a field star can lead to deduction of a spurious higher or lower extinction knot relative to the surroundings. This problem was not manifest on the He I or CEL images, since in general strong stellar absorption lines do not coincide with these lines.

Using a spectral library of observed Galactic stars, the spectra of the field stars over the nebula face were fitted. Subsequently the emission lines, which were affected by the presence of field star absorption lines, were analysed. Appendix A details this correction procedure.

3.2. Combination of line images

The signal-to-noise (S/N) of the emission line images is high over the bright core for the 40 s cube but low for all except the brightest lines over the halo; whilst the strongest emission lines are saturated over the bright core but well-exposed over the halo for the 101 s and 595 s cubes. With the aim of producing the deepest possible map of the extinction across the nebula, combination of the Balmer line images from each exposure level was made. The H emission lines images are well-exposed over the core in the 40 s images; the 101 s images, particularly for Hα, are saturated in regions over the core but well-exposed in the immediate surrounding; the images from the 595 s cube are saturated to radii beyond the core but well-exposed over the halo. The c(Hβ), log extinction at Hβ, image was computed separately for each exposure level using masked images and the resulting c(Hβ) images combined. (detailed in Sect. 4.1).

4. Imaging of physical conditions – Extinction, density, and temperature

4.1. Extinction mapping

From images of the ratios of Balmer and Paschen line fluxes compared to the Menzel & Baker (1937) Case B values, a map of the extinction across the nebula can be constructed. The value of the electron temperature, T_e, and electron density, N_e, must be provided, such as from the CEL indicators; for example, [S III] 6312/9069 Å and [Cl III] 5517/5538 Å, respectively. The combined c(Hβ) map used the three exposure levels to derive optimally exposed Hα and Hβ images that were converted to c(Hβ) by comparison to the Case B Hα/Hβ ratio: the 40 s cube for core region, using radius $r \leq 5.8''$; the 101 s cube for the annulus between core and halo, $6.0 \geq r \leq 10.2''$; and the 595 s cube for the halo $r \geq 10.4''$.

Based on first guess values of T_e and N_e of 10 000 K and 2000 cm^{-3} respectively for the core and 9000 K for the halo, the Case B value of the H line ratio was employed to calculate an initial c(Hβ) image. Then from the variation of T_e and N_e over the reddening corrected emission line maps (Sect. 4.2.1), simple mean values in two zones were adopted for calculating the final Case B Hα/Hβ ratio: inner ($r \leq 6.0''$) based on [S III] for T_e and [Cl III] for N_e; outer ($r > 6.0''$) based on [N II] T_e and [S II] N_e. Fig. 4 shows the resulting c(Hβ) image. Only small differences in appearance of this image were found if single constant values of T_e and N_e are used (10 000 K and 2000 cm^{-2} respectively) for the Case B computation; c(Hβ) means differ by <0.01 for a spatial mean value of 0.233. An extinction map was also constructed including Paschen 9, 10, 11 and 12 lines in addition to the Hα and

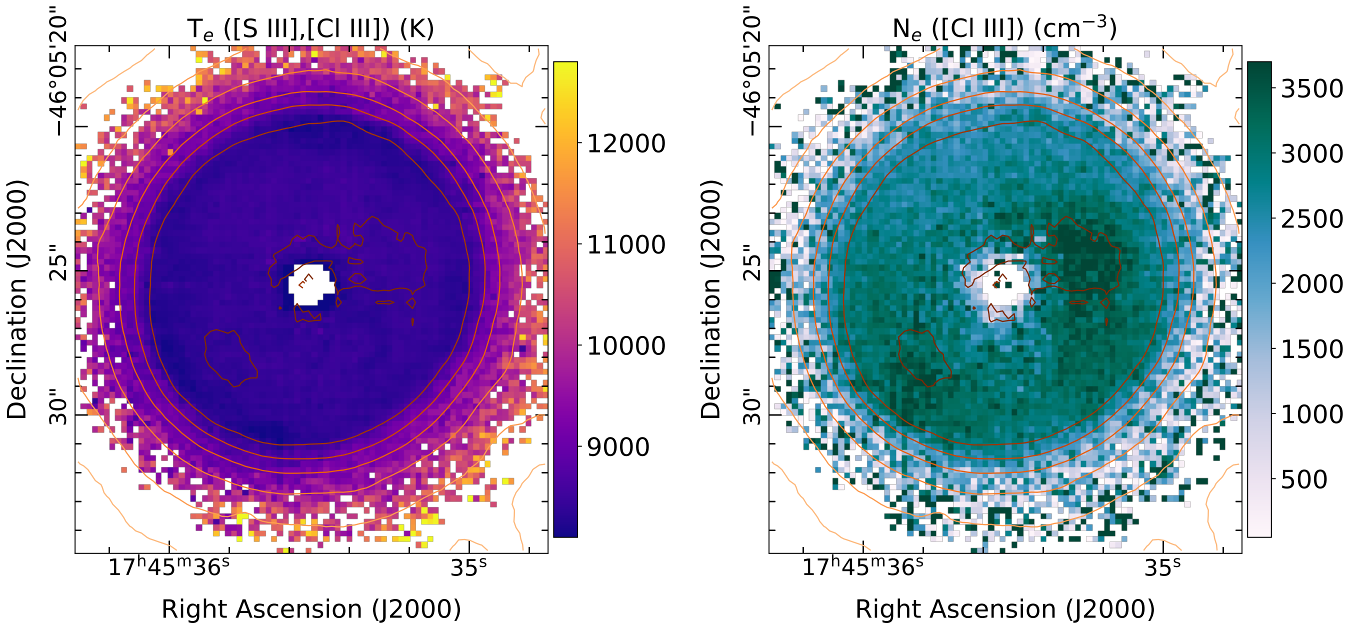

Fig. 5. T_e and N_e images for the higher ionization core area only, from [S III] 6312/9069 Å (left) and [Cl III] 5517/5537 Å (right). The colour bars indicate the T_e and N_e ranges and the Hβ line contour map is superposed and the cut-off in S/N is 3 per 0.2″ spaxel.

Hβ lines, and the results were again very similar, though systematically lower, within ±0.02 for the core and ± 0.04 for the halo. Given the lower S/N of the Paschen lines in comparison to the Balmer lines, this small difference was considered marginally significant.

All the emission line flux (and error) images were then dereddened using the c(Hβ) image (Fig. 4) and its corresponding error (the latter produced by propagating the flux ratio errors, but not the T_e and N_e errors).

4.2. Mapping of T_e and N_e

4.2.1. CEL diagnostics

The available CEL diagnostic ratios in the MUSE spectrum of Tc 1 are [N II] and [S III] for T_e, [S II] and [Cl III] for N_e. Whilst [Ar III] was also detected, the 5192 Å line was weak and has very low S/N, resulting in T_e values at the original spaxel resolution (0.2″) with large errors or values of the 5192/7136 Å ratio outside the theoretical range. All H, He and metal CEL ratio calculations were made with PyNeb (Luridiana et al. 2015) and relevant sources of the atomic data for the CEL computations are listed in Appendix B of Walsh et al. (2024). The c(Hβ) image (Fig. 4) was used to deredden all the emission line maps required for T_e and N_e measurement and the final maps were made by combining the 40 s images for the bright core, with the 595 s images for the surroundings and the halo.

Figure 5 shows the T_e and N_e images from [S III] 6312/9069 Å (left) and [Cl III] 5517/5537 Å (right) for the higher ionization gas. Figure 6 shows T_e and N_e images for the lower ionization gas from [N II]5755/6583 Å (left) and [S II]6716/6731 Å (right). All the maps were computed using the PyNeb *getCrossTemDen* code using the simultaneously computed N_e maps from [Cl III] and [S II] ratio images. Spaxels in these images without an N_e and/or a T_e value correspond to S/N values for the weak auroral lines in the diagnostic ratio below a cut-off value of 3. In the halo particularly, there are many spaxels with [Cl III] and [S III] lines below this S/N cut, but fewer for the lower ionization [S II] and [N II] line ratios.

Figure 7 summarizes the CEL diagnostics with a plot of the radially averaged profile with offset from the position of the CSt for T_e from [S III] 6312/9069 Å and [N II]5755/6583 Å, and N_e from [Cl III] 5517/5537 Å and [S II]6716/6731 Å. These are compared to the radial variation of extinction (c(Hβ) from Fig. 4) and the Hα surface brightness. For the diagnostics from [Cl III] and [S III], the line fluxes, and hence the S/N, were too low beyond the last plotted radial points for a meaningful comparison. The increase in T_e begins where the density drops (radius ∼5.7″), although N_e([Cl III]) appears to increase again beyond radii 7.5″, where however there were few spaxels with sufficient S/N to calculate N_e. This turning point in radial N_e and T_e values occurs as the extinction first decreases in an annulus around the core (see Figure 4 and Sect. 5.2 for a discussion). The extinction is also lower in the radial range 10–15″ but here the H lines were faint and there are many spaxels (particularly to the E and SE) without sufficient S/N to calculate c(Hβ).

4.2.2. ORL diagnostics

Diagnostic ratios of line and continuum from the recombination lines of H^+ and He^+ within the MUSE wavelength range can be used for electron temperature and electron density determination. These include the ratio of the high Paschen lines as an electron density estimator (cf. Zhang et al. 2004), the H I Paschen continuum jump at 8204 Å and the ratios of He^+ singlet lines, which are primarily sensitive to T_e.

H I Paschen Jump T_e. The Balmer and Paschen series continuum jumps for bound-free (b-f) transitions of H I are sensitive to electron temperature (Peimbert 1971) and Fang & Liu (2011) determined T_e from the Paschen Jump, normalizing the jump (defined as $F(8194\,\text{Å}) - F(8269\,\text{Å})$) by the Paschen 11 (P11) flux at 8863 Å. Walsh et al. (2018) (in Appendix) presented a measurement method suitable for multiple spectra of an IFU by

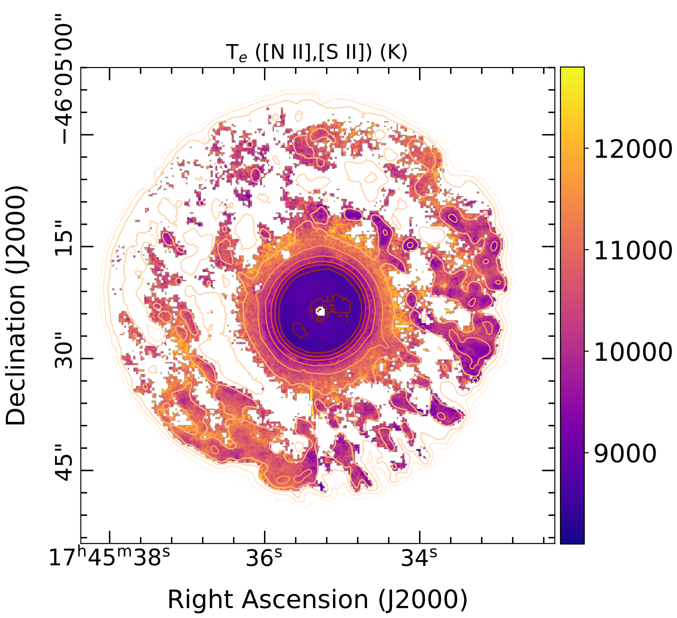

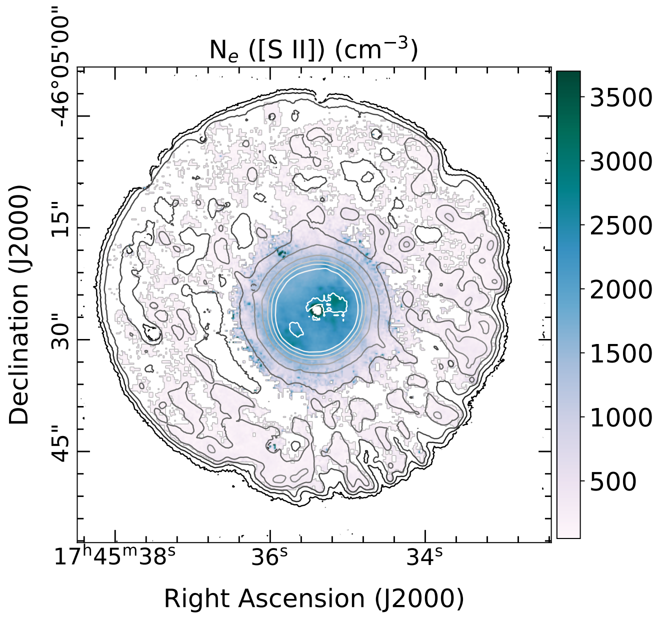

Fig. 6. T_e and N_e images of the entire nebula for the lower ionization medium from [N II]5755/6583 Å (left) and [S II]6716/6731 Å (right). The colour bars indicate the T_e and N_e ranges and the Hβ line contour map is superposed; the cut-off in S/N is 3 per 0.2″ spaxel.

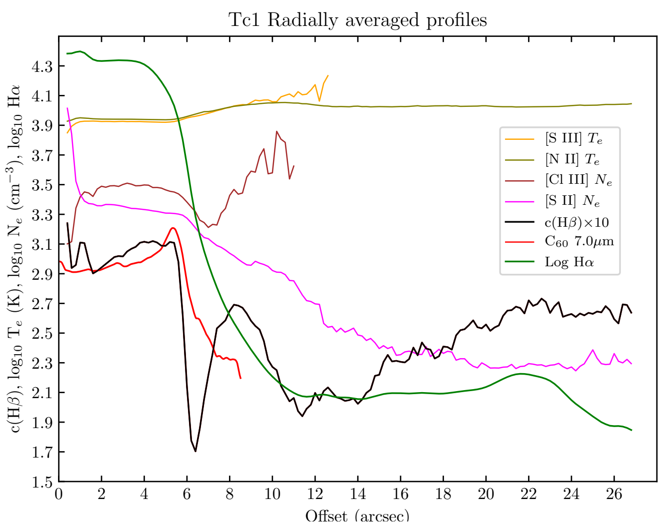

Fig. 7. Radial variation of the CEL diagnostics with the offset from the position of the CSt for T_e and N_e, which are both plotted as $\log_{10}$. For comparison the radial variation for c(Hβ), scaled by a factor 10 to be similar in values to $\log_{10}$ T_e and N_e, and the scaled $\log_{10}$ Hα surface brightness, are also shown. The low c annulus occurs between radii 6–7″. Also plotted (in red) is the $\log_{10}$ surface brightness profile of the C_{60} 7.0 µm band (erg cm^{-2} s^{-1} sr^{-1} × an arbitrary constant) for comparison (cf. Giese et al., in prep.). The C_{60} profile was however determined over a limited angular extent of 40°.

taking the mean continuum in several line-free windows on both sides of the Paschen Jump and a custom conversion of this difference with respect to the flux of the P11 line as a function of T_e, N_e and He^+/H^+.

Figure 8 shows the resulting map of the Paschen Jump (PJ) T_e. Since He^+ also contributes to the nebular continuum, the He ionic fraction was calculated from the maps of He I 6678 and 7065 Å line flux, but not 7281 Å on account of the anomalous flux of this line (see following subsection and below for details). Initial estimates of T_e and N_e for the dependence of PJ/P11 were taken as single values of T_e for the core (8900 K) and halo (10 750 K), and N_e of 2300 and 500 cm^{-3} respectively, based on the CEL T_e and N_e diagnostics (Sect. 4.2.1). There are two distinct zones: the bright nebular core with mean value of 7550 K and a root mean square (RMS) of 280 K (3 × 3σ clipped mean); the ring of higher T_e (broadly coincident with the annulus of low extinction) with a mean value of 11 500 K, RMS 1900 K. (The lower T_e values close to the CSt are caused by the presence of continuum from the wings of the point spread function (PSF) increasing the measured PJ blue-red continuum ratio.) The mean signal-to-error over the map, based on 100 Monte Carlo trials using the propagated errors on the measured PJ, is 12. Three small regions over the ring where there were background stars present had to be interpolated. Only over the bright core were the PJ T_e values lower than those for the CEL T_e; in the periphery the values were very similar.

He I T_e. Zhang et al. (2005) showed that the ratio of the two He I singlet lines 7281.4 and 6678.2 Å provides a suitable diagnostic of the He^+ electron temperature and thus a useful ORL temperature. The determination of T_e from 7281/6678 Å was based on emissivities from Porter (Porter et al. 2012, 2013) tabulated for 5000 < T_e < 25 000 K. The observed dereddened He I 7281/6678 Å ratio was converted to T_e and N_e by minimizing the residuals with the theoretical ratio. First guess values of T_e and N_e were taken as single values for the core and halo based on the CEL T_e and N_e, as in the calculation of PJ T_e (see previous subsection). The He I ratio is much more sensitive to T_e than N_e and the initial estimate of T_e was adopted to compute the emissivities; N_e was held fixed within narrow constraints during the minimization.

Figure 9 shows however that in an annulus beyond radius 5.5″ from the CSt, the observed He I 7281/6678 Å ratio exceeds the allowable range of this ratio of 0.13–0.31 across the range T_e 5000–25 000 K and log N_e 1–7. Over the core, within radius 5.5″, the computed mean value of He I T_e was 10 650 ± 450 K (3 × 3σ clipped mean), but no value could be computed for the

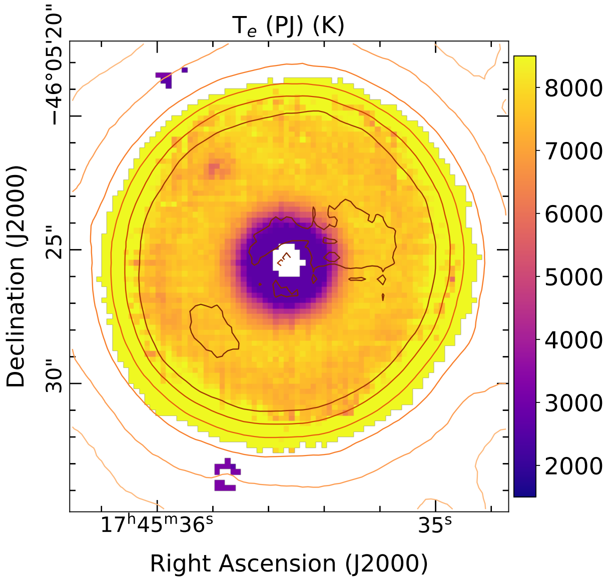

Fig. 8. Map of T_e for the core region only, derived from the Paschen continuum jump at 8250 Å ratioed by the dereddened H I Paschen 11 (8862.8 Å) emission line strength. Initial estimates of T_e and N_e from the CEL diagnostic ratios (Sect. 4.2.1) for calculation of the dependence of PJ/P11 on T_e were employed. The contours are from the Hβ image (Figure 1) and the cut-off is at S/N of 3 per 0.2″ spaxel.

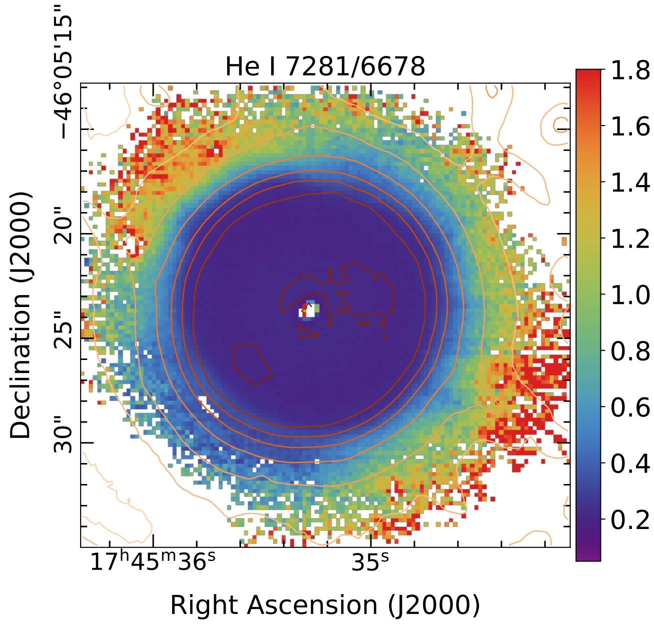

Fig. 9. Image of the Tc 1 core region for the ratio of the fluxes of the He I 7281 and 6678 Å lines. Spaxel values above 0.31 are outside the feasible range of the He I ratio, indicating a possible contaminating line in the region outside of the bright core. The contours are for the Hβ flux.

region outside this radius. The most probable explanation is that another emission line, close to 7281 Å but within the spectral resolution of MUSE at this wavelength (~2.8 Å), contaminates the He I line flux outside the extent of the bright core.

In order to investigate the possibility of a contaminating line close to He I 7281 Å, VLT X-Shooter (Vernet et al. 2011) spectra (Proposal ID: 097.D-1033(A), PI J. Cami) were examined. There are two slits with differing PA's including the CSt and extending beyond the outer edge of the core, so into the region where He I 7281 Å is enhanced. The much higher spectral resolution of X-shooter (~ 10 000) than MUSE could allow a contaminating line within ~0.5 Å of 7281 Å to be revealed. These spectra were reduced and the spectrum around 7280 Å examined. No evidence of a resolved nebula line close to 7281 Å was found, nor any suggestion of a broadening of 7281 Å compared to the nearby He I 6678 Å line. Although the X-Shooter slit only covered a region slightly beyond the core, an increase in 7281/6678 Å ratio is visible towards the edge of the slit (although the S/N is low). The conclusions from the MUSE spectra that there is indeed an enhancement at 7281 Å outside the core, and above the expected He I theoretical ratio to 6678 Å, is thus confirmed.

In the Atomic Line List (van Hoof 2018), the closest feasible nebula line was [Fe II] 7281.66 Å displaced only 0.35 Å from the He I 7281.31 Å line. In order to check if this line could represent a significant contamination to the He I flux, the deep spectrum for IC 418 (Sharpee et al. 2003) (a nebula with similarities to Tc 1 in terms of ionization and fullerene detection) was consulted for detected [Fe II] lines. The strongest [Fe II] line in IC 418 in a relatively uncrowded region of the MUSE spectrum is 5495.8 Å with a dereddened line strength 0.015 (Hβ=100), although listed by Sharpee et al. (2003) as blended with N II[3]. Extracting a spectrum of Tc 1 in the area of the possible contaminated He I line, reveals a detectable line at 5496 Å with a dereddened strength of 0.015 that is remarkably similar to the value for IC 418. However, given that the ratio of [Fe II] 7281.7/5495.8 at the T_e and N_e measured for this region (see Table 2) would be 0.003, any contamination of 7281 Å by [Fe II] is negligible. Since a viable contaminating line to He I 7281 Å could not be identified, we infer that the origin of the 7281 Å enhancement in the outer annulus is unresolved based on the analysed observations.

5. Discussion

5.1. Emission line morphology

Already known from previous imaging (e.g. Corradi et al. 2003) was the strong contrast between the almost circular bright core of diameter ~12″ (0.22 pc) and the halo, 55″ in size. The mean contrast in Hα surface brightness between the core and the halo is 490 (530 for the dereddened image). While the CSt is situated at the centre of the core nebula, the circular halo is displaced relative to the CSt in PA ~15° by 2″ (this is particularly noticeable in the extinction map, Fig. 4). The Gaia stellar proper motion (pm) direction is towards PA 194.09°; from the offset of the halo to the N, it is apparent that the CSt and core nebula together have a motion relative to the halo. If the halo is an older structure, such as the remnant of the AGB envelope, then a modest plane of the sky differential velocity between the CSt and the halo of <1 km s^{-1} in 5×10^4 yr (indicative difference in age between the AGB halo and current CSt) could account for the observed CSt-halo offset. Given that the proper motion is in almost the opposite direction to the halo extension, there may be an effect of compression of the halo in the direction of the pm, and/or extension in the opposite direction depending on the ISM pressure.

The core nebula has considerable structure (Figs. 1, 2), with the individual features marked in Figure 1, right. The Hα surface brightness of the central 12×12″ region is shown in

[3] The [Fe II] 5035.1 Å line is however stronger than 5495.8 Å but has several nearby lines at MUSE resolution, making it more difficult to fit.

Table 2. Parameters and diagnostics for region spectra.

Region name	Radius (″)	Area (″²)	c(Hβ)	Dered F(Hβ) (cgs)	[S II] N_e 6716/6731Å (cm^{-3})	[N II] T_e 6548+83/5755Å (K)	[Cl III] N_e 5517/5537Å (cm^{-3})	[S III] T_e 9068/6312Å (K)
Core	4.8	33.44	0.32	1.19e-11	2100	8700	2900	8400
Low c	6.5	36.32	0.18	8.30e-13	1800	9700	2000	9100
Halo	10.3	246.2	0.24	2.63e-13	600	11 100	680	10 800
Total	<27.2	2228.6	0.31	4.39e-11	1900	9400	2700	8600

Notes. All N_e and T_e values were calculated with PyNeb. See Appendix E for the line fluxes on which these diagnostics were based.

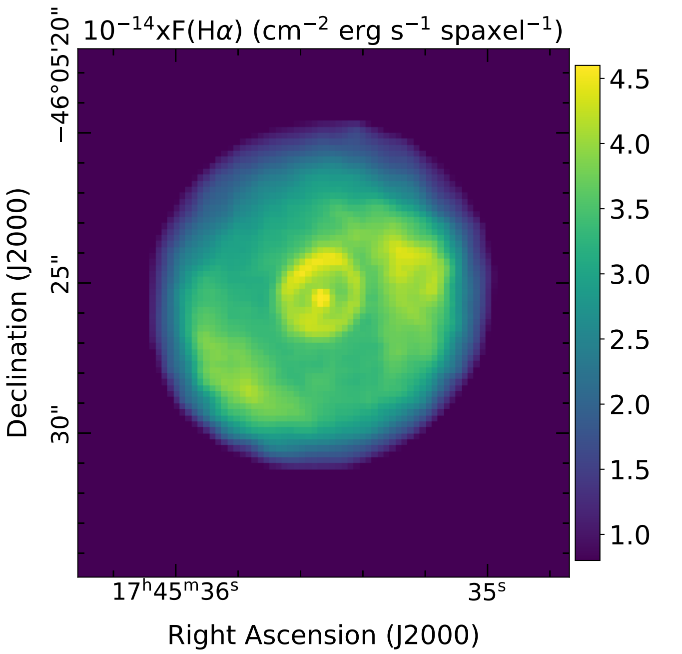

Fig. 10. Expanded image of the core region of Tc 1 in Hα surface brightness (10^{-14} erg cm^{-2} s^{-1} spaxel^{-1}).

Figure 10, emphasising the bright core region only. The higher ionization morphology, typified by [O III] is brightest near the CSt and steadily declines at larger radii of the core, and into the halo. The bright core is close to circular and the FWHM is about 10.8″ and there is a distinct inflection in the decrease of the Hα surface brightness at radius 6.2″ from the CSt, giving an outer diameter of the core of 12.4″ (see also Fig. 7). Closest to the star is an elliptical ring structure of axis lengths 2.8×2.2″, position angle (PA, measured N through E) of the major axis 160°, with centre offset by 0.3″ to the NW from the position of the CSt; the NE rim is notably brighter. This ring is visible in the permitted lines (H and He), [O III], and [O II] but not [N II] and its PA is displaced by ∼30° from the PA of the proper motion of the CSt. The ring is also enhanced in the extinction image (Fig. 4) by about 0.03–0.04 dex relative to the immediate surroundings, implying some dust content.

Outside of this ring beyond >2″ radii, the surface brightness is lower in the H and low ionization emission but then rises again in a horseshoe shape extending from the NW around to SE, with the NW region brighter and composed of multiple knots, while that to the SE has a single bright knot. The horseshoe feature shows two regions of compact emission peaks (‘knots’) to the NW (brighter knots) and SE, strongest in lower ionization and in [O I], but not seen in [O III]. There are hints of arcs of emission extending from the central ring – the NW one extends inwards to the ring while that to the SE is more distinct. The contrast of these knots is greatest in [O I] emission where the large-scale background emission is very low. Some of the knots to the NW and the brightest one to the SE have been shown by Bouvis et al. (2025) to display enhanced metal line emission, characteristic of Low Ionization Systems (LIS) found in some PNe. A difference in radial velocity of these knots from the surrounding large scale emission is apparent, despite the low spectral resolution of MUSE spectra: from [O I] (for the 595 s cube), the NW knots show velocities relative to systemic of about +20 km s^{-1} and the SE knots velocities −15 km s^{-1}. Given the low ionization of these features and their velocity offsets with respect to systemic, it is suggested they compose an outflow feature that lies outside the core and probably in the halo. Higher resolution spectra of these low ionization knots relative to their surroundings would be required to better establish their location.

Outside the core there is a shoulder in the H emission surface brightness, between radii 6.4″ and 8.0″ leading to the halo where the surface brightness no longer declines ($r \gtrsim 10''$); see Fig. 1. The halo can be broadly characterized as low ionization with only very faint and featureless emission of O^{++} (see Fig. 2). Outside the core there is a ring of lower emission in Hα and [O II], [N II] about 3–4″ in width (more extended to the SW) enclosed by many filamentary structures. Protruding from the core are two spikes at PA 70 and 240° but neither of the major axes of these spikes pass through the position of the CSt; nor does the line joining the origins of these spikes at the edge of the core pass through the CSt. The spikes are visible in H lines and lower ionization but only the eastern spike (PA 70°) on the extinction image and at [O I]. Their nature and origin remain unexplained, but again higher spectral resolution may assist in detecting a velocity offset or gradient to these features. The outer filaments are often arcs but there are some radial features; all are characterized by lower [N II]6583 Å/Hα than the large-scale extra-filament emission (ratio lower by <0.5 compared to the mean of 1.00). The brightest feature in the halo is the wedge-shaped knot to the WSW at Δα, Δδ −21, −5″ relative to the position of the CSt, but this feature is only 10% of the peak flux of the knots in the core already discussed. It is faint in [O I] 6300 Å emission and the [N II]6583 Å/Hα ratio is low, implying different properties between the core and halo knots. The filaments seen in emission are visible in extinction with an increase in c(Hβ) with respect to the mean of the halo (c = 0.244) of up to 0.2 dex, indicating considerable dust content. None of the spikes or outer filaments show convincingly differing velocities from the systemic velocity.

The outer edge of the halo appears sharp to a limiting radius of ∼27.8″ (Fig. 1), based on the brightest emission

Table 3. Adopted parameters of the nebular continuum fits to Tc 1 region spectra.

Annulus	c(Hβ)	Dered F(Hβ) (erg cm^{-2} s^{-1})	T_e H I (K)	T_e He I (K)	N_e (cm^{-3})	He$^+$/H$^+$
Core	0.31	1.19×10^{-11}	8570	9150	2200	0.092[1]
Low c	0.21	8.55×10^{-13}	9250	10 070	1800	0.074[2]
Halo	0.26	2.74×10^{-13}	11 100	11 100	670	0.049[3]
Total	0.31	4.77×10^{-11}	8550	9150	2410	0.092[4]

Notes. [1] He$^+$/H$^+$ based on He I 6678 Å/Hβ and 4922 Å/Hβ of 3.68 and 1.25, (I(Hβ)=100.0), with mean He$^+$/H$^+$ from [Cl III] and [S III] N_e and T_e, weighted 3:1 respectively. [2] He$^+$/H$^+$ based on He I 6678 Å/Hβ and 4922 Å/Hβ of 2.85 and 1.02. [3] He$^+$/H$^+$ based on He I 6678 Å/Hβ of 1.93 only and [Cl III] and [N II] N_e and T_e. [4] He$^+$/H$^+$ based on He I 6678 Å/Hβ and 4922 Å/Hβ of 3.530 and 1.175. The T_e values for H I are based on the temperature sensitive ratio [N II]5755/6383 Å and N_e values are a mean from the density sensitive ratios [S II]6716/6731 Å and [Cl III] 5517/5537 Å. The He$^+$/H$^+$ number ratios have been derived from recombination theory after correcting the H I line flux for collisional excitation contributions, using the formulae of Kingdon & Ferland (1995).

line, Hα. However, since the outer edge of the emission was actually defined by a S/N cutoff in the line flux detection, and in addition the outer edges of the field were employed for sky background subtraction (Sect. 2), the reality of an intrinsically sharp boundary to the nebula cannot be confirmed from these observations. At lower surface brightness the halo extent may be more than 28″ – deep, wide-field imaging is required to check this possibility. If real, the boundary could occur between the halo (mean density $N_e \sim 600$ cm^{-3}, Table 3) and the surrounding ISM (density-bounded), or the limit of photoionization for an ionization-bounded halo.

Based on the current expansion velocity of the low ionization species of ≃20 km s^{-1} from Aleman et al. (2019), the core of radius 6.2″ has a dynamical age of 5200 yr. To estimate the dynamical age of the halo requires an expansion velocity that has not so far been measured (the emission lines over the halo are spectrally unresolved by the MUSE data). Assuming the halo is the remnant of the AGB wind, then the compilation of Knapp et al. (1998) provides a mean wind velocity of 13 km s^{-1} based on their observations of 13 C star AGB envelopes (mean 12.8 ± 4.8 km s^{-1}). With a radius of 28″, the dynamical time of the Tc 1 halo is then 36 000 yr.

5.2. Dust extinction structure

The wealth of detail in the extinction image in Fig. 4 reveals for the first time the complexity of the dust distribution, in the case of Tc 1 equalling or even surpassing the morphological detail in the emission line imaging. The structure to the extinction image in Fig. 4 can be broadly grouped into three areas: the bright core; the annulus between the core and faint halo; and the halo itself. The mean c(Hβ) value over the core is 0.306 (std 0.023) but there is a compact region to the WNW and a ring from PA 80–250° around the outer periphery of the bright core (radius 5.9″) with values elevated up to c=0.34. The peak c(Hβ) value occurs at the position of the CSt (maximum 0.59). At the centre is a slightly elliptical ring of enhanced extinction (by c(Hβ) of 0.02) that is spatially coincident with the ring of enhanced emission mentioned in Sect. 5.1.

Over the halo (radii > 9.2″) the mean c(Hβ) value is 0.236 ± 0.097, but there is also structure with two distinct ridges to the W and SW plus a radial feature to the E, together with more compact c(Hβ) enhancements (larger in size than the PSF). However most unusual is the annulus of lower c(Hβ) values around the periphery of the bright core (radii 5.9–6.9″). This feature in itself is not unique and from the MUSE observations of NGC 7009 (Walsh et al. 2016) a narrow region of lowered c(Hβ) values (Δ c(Hβ) ∼ 0.03) was found around the bright inner shell (see their Fig. 1). Here however, when the interstellar medium (ISM) extinction in the direction of Tc 1 is taken into account (E_{B-V} = 0.158 from Schlegel et al. (1998), c(Hβ) ∼ 0.23 for a Howarth (1983) reddening law with R_V=3.1, and a value very close to the mean for the halo), the annulus displays 'negative' extinction, with values to −0.07 below the ISM value (corresponding to Hα/Hβ ratio = 2.99, which is well above the expected Case B value, so not an extinction deficit in an absolute sense). This unusual structure, with seemingly negative values of extinction over an area ∼36″^{2} surrounding the bright halo is unprecedented in a PN.

Given the unusual nature of this localised extinction behaviour it is valid to question whether the ISM value of extinction is perhaps too high and indeed corresponds to the low value observed in the annulus. The values from Schlegel et al. (1998) and G-TOMO (Vergely et al. 2022) however agree closely and are concordant with the extinction inferred from the strength of the Diffuse Interstellar Bands (DIBs) by Díaz-Luis et al. (2015). The agreement with these ISM values and the mean extinction over the halo, where N_e is low and, apart from the noted extinction features, the extinction is rather uniform, tends to argue against a lower ISM extinction. An investigation into the extinction towards the stars in the halo of Tc 1, which were used to correct for the effect of their absorption lines on the emission line maps (Sect. 3.1), might be productive.

In Fig. 7, the radial profile of the C_{60} 7.0µm band from Giese et al. (in prep.) is also included on the plot for direct comparison with the visual extinction c(Hβ) and log$_{10}$ T_e and N_e radial profiles. However the C_{60} profile is only formed over the limited range of PA's of 240–280° available from the James Webb Space Telescope (JWST) Mid-Infrared Instrument (MIRI) observations (Giese et al., in prep.); the plotted profile is the mean of four profiles over 10° sections. The extinction displays a slight peak at offset 5.4″, coincident with the peak emission of the C_{60} shell, although too much should not be drawn from this comparison, given that the extinction profile is from a complete radial profile and showed a slight elevation at this radius for PA 80–250°. However beyond the peak in extinction and C_{60} 7.0 µm emission, both profiles decline, supporting links between the extinction and C_{60} emission structures.

The low extinction annulus occurs where N_e starts to drop, T_e starts to rise into the halo and C_{60} emission drops. This concurrence of four indicators of gas and dust properties, which all change within a short radial extent, points to linked physical conditions at the edge of the inner core. The changes in dust extinction properties, which can be interpreted as a higher proportion of small dust particles or of larger particles, point to dust processing in this zone. Two possibilities are suggested to cover these cases: destruction or ablation of dust could occur at the shock front ahead of the outer rim of the higher density core nebula, leading to the low extinction annulus; ablation of larger dust particles that are present in the halo, occurs as the ionization shock front moves outwards, resulting in a higher proportion of smaller grains than inside the ionized core. The increase in T_e can be linked to the decrease in N_e in this annulus (see also Table 3), either through a change in ionizing photon optical depth or radiation hardening (Sect. 5.4); whether these changes in physical conditions are linked to the dust is not clear. If dust processing does occur, as strongly suggested, then this may provide increased heating; a detailed model would be required to determine if this mechanism could also contribute to the increase in T_e.

5.2.1. Instrumental effects on extinction determination

Apparent negative extinction should not exist under standard nebular conditions in a PN, so in order to verify an intrinsic effect within the nebula, possible observational or instrumental artefacts need to be scrutinised. The region of the extinction deficit occurs in a narrow radial zone just outside the bright core (radii 5.8–7.2″ from the CSt) where the Hα and Hβ local gradients in surface brightness drop steeply (e.g. Fig. 7). The observed spatial PSF is affected by both atmospheric effects and transfer through the instrument; the former has a well-known decrease to longer wavelengths (Fried 1966), so even without instrument contribution, the radial profile in the blue is broader than in the red. Since the line surface brightness of the core is much higher than in the range of radii under scrutiny (by a factor ~130 for the radially averaged profile), then light in the PSF wings can be scattered from the core into the surroundings, enhancing the blue flux and hence Hβ. Just such an enhanced Hβ flux could then cause a lower extinction measured from Hα/Hβ. If the instrument contribution to the PSF was also broader in the blue, this would enhance the trend resulting from the atmospheric PSF; any significant contribution in the wings of the PSF, say >1.0″ would preferentially scatter blue light from the core into the surroundings, 1–2″ offset from the fairly sharp edge to the core (radius 5.5″). Walsh et al. (2016) also checked if this explanation could account for the (smaller) extinction decrease outside the bright shell in NGC 7009; it was discounted as the surface brightness contrast was lower. The chromatic character of the PSF can be quantified by taking an observed PSF from one or more star images, or a model PSF, and deconvolving the observed Hα and Hβ images. Appendix B describes these experiments.

The conclusion of these tests was that, while there may be an influence of the PSF chromaticity on the measured Hα/Hβ in the range of radii adjacent to the bright core, it cannot explain the drop in extinction to values below the ISM value. Therefore an astrophysical explanation of the extinction deficit is mandated. For example, a process to locally alter the extinction law, or optical depth effects on the Hβ and/or Hα line flux emitted towards the observer, must be invoked. The latter can be strongly excluded since there were no strong changes in physical conditions over the radii in question (see Fig. 7), other than a decrease in N_e by ~2000 cm^{-3} and an increase in T_e of ~2000 K (Fig. 6). For these modest changes in physical conditions, no large change in H emissivities or optical depths is expected and no reason to suspect departure from Menzel & Baker Case B. In addition, the physical conditions were very similar to those over the halo and the extinction (above the ISM value) is low (and positive), which is as expected for the low gas density, and hence low dust density assuming constant gas-to-dust mass ratio.

5.2.2. Dust radiative transfer effects

Given that the dust extinction image (Fig. 4) already shows gross effects of spatial variation in extinction, as between the core (c=0.31) and the halo (c=0.24), the role of dust transfer would appear to be a promising candidate to explain the low extinction annulus. Dust particles absorb radiation and scatter it out of the incident direction and the combined effect produces extinction. If there was a local volume within a nebula where the dust particles were smaller, the resulting scattered light would be bluer than in the rest of the nebula; then scattering of Hβ would be elevated relative to the surroundings, which leads to a decrease in observed Hα/Hβ even though the mass of the dust column may not spatially vary.

A possible mechanism to produce this result could be sputtering of the bulk larger grains to produce a local enhancement in smaller grains (or even grains with a different composition). The threshold relative velocity for grain sputtering by atoms and ions is > 50km s^{-1}, for a range of grain types (Jones et al. 1994). However based on the velocity field from Aleman et al. (2019), such gas velocities are unlikely to be present in Tc 1. Grain fragmentation as a result of grain-grain collisions has a much lower threshold velocity (Kirchschlager et al. 2019, Table 2) and such fragmentations produce a shower of smaller particles – so this could provide a more likely mechanism for producing smaller grains than sputtering. A possible mechanism for producing grain-grain velocity differences could be provided by differential motions between grains in the bright core and those beyond. At the boundary of the bright core, where the ion density, and therefore the plasma drag, drops significantly, grains near the boundary may overshoot into the lower density nebular material and thereby collide with the existing grains in this region.

In order to explore the feasibility of smaller grains causing the localised lower extinction, a simple 3D dust scattering model was produced and details of the model and the approach are given in Appendix C. An annular reduction in extinction at the outer edge of the bright core could be produced if there was a shell of dust grains scattering light from the bright core; the line of sight extinction over the core itself would also be affected by this scattered component, but the effect is very small (since the scattering column is short). It is curious that the extinction from Hα/Hβ in the vicinity of the CSt (Fig. 4) is lower than measured to the CSt from stellar continuum fitting (see Sect. 5.3) by 0.086 (c=0.299 from Hα/Hβ in the 12″^{2} around the CSt compared to c=0.385 for the CSt spectral energy distribution [SED] fitting). The difference implies that there is small scale extinction along the sightline to the CSt, perhaps local to the CSt; this suggestion can be checked by comparison to infrared dust mapping.

The dust scattering models described in Appendix C were inconclusive in terms of explaining such a large apparent decrease in the extinction in the c(Hβ) annulus, although they are indicative that a smaller effect could be produced (δc ~ 0.03). However the models were confined to well-behaved dust (spherical particles of amorphous carbon or fullerene (assumed C_{60}) molecules as very small grains). More complex dust species and distributions (ellipsoidal or cylindrical grains, mixed C grain types, perhaps including fullerene admixture) should be considered. The James Webb Space Telescope near- and mid-infrared imaging and spectroscopy (Cami et al., in prep) can provide further data on the spectral and spatial properties of the dust and fullerene emission. It is already clear that the peak of the fullerene emission (offset ∼4.5–5.0″) occurs inside the ring of the apparent extinction deficit (5.9–6.9″, Fig. 4), so a direct association of a shell of fullerene emission with the region of lower extinction is not indicated.

An alternative to small dust grains, giving enhanced scattering in the region outside the core of Tc 1, is large grains. Here the change is in the extinction properties: for larger grains the wavelength dependence of the extinction is flatter. The extinction properties can be described by the value R_V, the ratio of total (A_V) to the wavelength selective extinction (e.g. E_{B-V}). It has been found that larger values of R_V than the typical Milky Way value of 3.1 are characteristic of larger grains (for a single size grain, $1/R_V \propto$ slope of extinction curve between B and V, Draine (2011)). Large values of R_V have been measured in star-forming regions, such as H II regions (e.g. Rogers et al. 2024) and in the young starburst galaxy NGC 5253 (Pruijt et al. 2026). If the region outside the Tc 1 core was populated by a greater fraction of large grains than within the core, then a higher value of R would be required to determine the extinction from the observed to Case B Hα/Hβ ratio. Then on account of the less steep extinction law compared to the core, the resulting c(Hβ) value for the region adjacent to the core would have a similar value to the region for the halo, and to the interstellar extinction, obviating the need for a deficit in extinction.

A simple experiment was conducted on the Region spectrum for the low c annulus (Sect. 5.4), determining the extinction from the observed Hα/Hβ of 3.29 with differing values of R_V than used for constructing the extinction map (Fig. 4) with R_V=3.1. For these tests, the Cardelli, Clayton & Mathis (Cardelli et al. 1989) extinction law, a parameterization that is dependent on the value of R_V, was used. For example, the calculated value of c(Hβ) with R_V=5.0 was 0.25 for the low c annulus, actually larger than the interstellar extinction value of 0.23. The resulting extinction map with a confined annulus of R_V=5.0 grains would then show a flatter extinction from the outer rim of the core to the outer edge of the halo. If the dust grain properties were so spatially stratified, then other regions could show similar effects – such as part of the halo ($10 < r < 14''$) where c(Hβ) is low relative to the interstellar value (see the profile in Fig. 7). Conversely if such a large value of R_V was applicable in the core, then c(Hβ) would be higher than computed with R_V=3.1.

5.3. Central star

The bright central star (CPD −46° 11 816) was well detected in the shortest exposure cube and allows an investigation of its spectral characteristics over the MUSE wavelength range 4700–9300 Å.

5.3.1. The MUSE spectrum of the central star

The spectrum of the CSt was extracted from the 40 s datacube (the only exposure level where the star image was not saturated) by summing an almost circular area of 4.68″^{2} centred on the star and subtracting the local emission as the mean in four cardinal regions around this area (annular radius 2.6″), encompassing an area of 25.44″^{2}. Figure 11 shows the resulting observed spectrum (in black). It was apparent that positive residuals of the strongest lines (H and [O III]) remain after this subtraction; the H lines

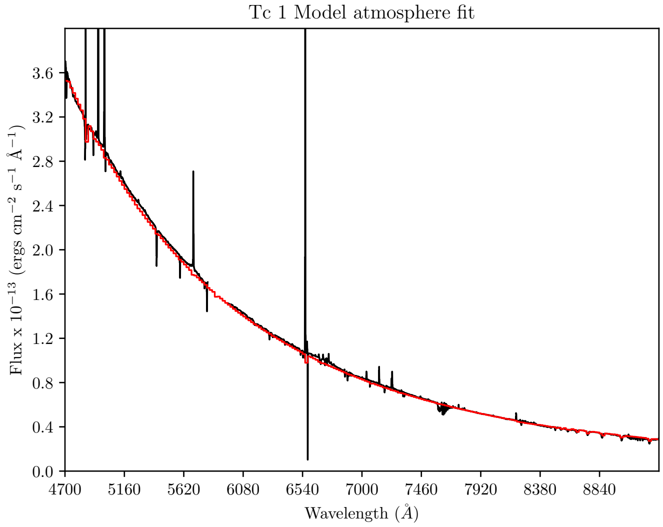

Fig. 11. MUSE spectrum of the CSt of Tc 1 extracted from the 40 s cube. The black line shows the dereddened spectrum (E_{B-V} = 0.265, c(Hβ) = 0.385) and the red line the matched Kurucz 9 LTE model atmosphere for T_{eff} = 31 000 K, log g = 3.5 (Castelli & Kurucz 2004). See text for details.

show a 15% enhancement, the [O III] lines a 130% increase relative to the mean background annulus flux. Thus excess emission close to the CSt, stronger for higher ionization species, is spatially resolved. From the MUSE extinction map (Fig. 4) there appears to be extra extinction to the CSt relative to the surroundings – the integrated c(Hβ) value in an aperture of 0.4″ radius is 0.43 (0.46 from the integrated Hα/Hβ flux ratio in the same aperture) and the peak value is 0.59, relative to a mean value for the surroundings of 0.30. However given the problem of fitting the narrow Hβ stellar absorption line profile under the emission line (and to a lesser extent the Hα line), the enhancement in extinction is quite uncertain.

Another approach was to fit the continuous spectrum of the CSt with a model atmosphere and search for the extinction and stellar (T_{eff}, log g) combination that best matches the observed stellar flux distribution. From their CLOUDY (Ferland et al. 2017) photoionization modelling of Tc1, Aleman et al. (2019) found a blackbody best match for T_{eff} between 30 000 and 32 000 K. For the photoionization modelling of Tc 1, Otsuka et al. (2014) adopted T_{eff} = 34 060 K and log g = 3.4. From their NLTE stellar atmosphere modelling of the IUE high resolution ultra-violet (1150–2000 Å) spectrum of the CSt, Pauldrach et al. (2004) found a best fit for T_{eff} = 35 000 K with log g = 3.62.

Here fits to local thermodynamic equilibrium (LTE) spectral energy distributions (SEDs) from Kurucz 9 Castelli & Kurucz (2004) model atmospheres for (a) T_{eff} = 31 000 K, log g = 3.5 and, (b) T_{eff} = 35 000 K, log g = 4.0 were tested. The MUSE CSt spectrum was dereddened over a small grid of E_{B-V} values using the Howarth (1983) Galactic reddening law with R_V = 3.1 and then normalizing the two alternative Kurucz models to each dereddened CSt spectrum. The most suitable matches were selected by examining the blue-to-red slopes of the residual of the Kurucz model subtracted from the dereddened CSt spectrum. The residuals turn out to be very sensitive to the value of E_{B-V} used for the dereddening. The 31 000 K, log g 3.5 model, dereddened with E_{B-V} 0.265 gave the most satisfactory fit; E_{B-V} values differing by ±0.005 showed residuals increasing and decreasing, respectively, towards the blue. For the case of the 35 000 K log g 4.0 model SED, again E_{B-V} of 0.265

produced the flattest residual slope, although the residuals were not as smooth as for the 31 000 K Kurucz model. This led us to adopt the 31 000 K, log g 3.5 model as the most reliable. This value compares closely with the range 30 000–32 000 K found by Aleman et al. (2019) from photoionization models. Figure 11 shows the match of this model atmosphere to the spectrum dereddened with E_{B-V} = 0.265 mag. For the adopted Galactic reddening law, the corresponding value of c(Hβ) is 0.385, thus confirming the nebula analysis that there is an extra component of extinction towards the CSt above that for the ionized gas alone, although not as large as derived above from the nebular extinction mapping. It is notable that this increased line-of-sight extinction to the CSt is larger than for the projected elliptical ring (discussed in Sect. 5.1), so they may not necessarily be part of the same structure.

For a distance of 3.53 kpc, the luminosity corresponding to the normalized Kurucz 9 LTE model atmosphere is 8150 $L_\odot$. For this temperature and luminosity, the star is on the horizontal post-AGB track corresponding to a Solar metallicity initial mass of ~2.0 $M_\odot$ (Miller Bertolami 2016). This mass estimate for Tc 1 is concordant with the mass range (1.5 $M_\odot$ < M ≲ 4–5 $M_\odot$ at Solar metallicity) for production of a carbon-rich nebula (Marigo et al. 2003). However the dynamical expansion age of the nebula (Sect. 5.1) is longer than predicted for a 2 $M_\odot$ Solar abundance AGB star at T_{eff} = 31 000 K by the Miller Bertolami (2016) tracks (<500 yr). Either the expansion velocity was higher in the past and has slowed, or the star has a lower mass with correspondingly slower evolution time, or both.

5.3.2. The central star spectral type

CPD −46° 11 816 has been observed with the VLT Ultra-Violet Echelle Spectrograph (UVES) at a spectral resolving power of R = 37 000 (Progam ID: 095.D-0432(A)) and an extensive study of the DIBs was published (Díaz-Luis et al. 2015). The spectra were retrieved from the ESO Archive with the aim of determining the spectral type of the CSt. We also had access to a spectrum from July 1980 taken on the 3.9 m Anglo-Australian Telescope with a resolving power of 9000 over just the 4230–4730 Å region. This spectrum showed the stellar 4634, 4640 Å N III doublet in emission and no stellar He II 4686 Å emission, implying an O(f) spectral type. From the UVES (3281–4530 Å) spectrum, the equivalent width (EW) of the He I 4471 Å line[4] is 690 mÅ, while the AAT spectrum gives an EW of 550 mÅ for the He II 4542 Å line. The 4471/4542 Å EW ratio of 1.25 implies a spectral sub-class of O7.5, according to Table 3 of Conti & Alschuler (1971) and Fig. 1 of Martins (2018) (assuming that the spectrum did not change between 1980 and 2015). A high mass Milky Way star with an O7.5I spectral type should have T_{eff} = 34 000 K (Massey et al. 2005, Table 9), similar to the estimates of 35 000 K (Pauldrach et al. 2004) and 30 000–32 000 K (Aleman et al. 2019). We conclude that a spectral type of O7.5I(f) best matches the available stellar spectra.

5.4. Region spectra

In order to check the controversial result of an extinction deficit in an annulus around the Tc 1 core and explore if other effects were apparent in the line and continuum emission, and diagnostics (cf. Fig. 7), region spectra were constructed summing large numbers of spaxels over selected regions. Such spectra have the advantage of high S/N, bringing a check on areal analysis based on spaxel data only. Four regions were selected:

- an annulus over the bright core centred on the CSt (radius inner, outer, mean 4.4, 5.2, 4.8″, area 33.44″^{2});
- an annulus containing the region of low extinction (spaxels with c(Hβ) < 0.22), inner, outer, mean radii 6.0, 6,9, 6.45″; this is an irregular annulus of 36.32″^{2};
- a wider annulus over the faint halo (radii 8.6, 12.2, 10.4″, area 246.24″^{2});
- total nebula (area 2228.56″^{2} based on detected Hα flux >1.0×10^{-17} erg cm^{-2} s^{-1} spaxel^{-1} and excluding 5.08″^{2} over the CSt).

The shape of the first three regions was chosen as an annulus, so that any radial variation of parameters with respect to the position of the CSt could be examined. The mean radii of these four regions and their areas are summarized in Table 2.

5.4.1. Line emission

The extinctions (from Hα/Hβ compared to Case B at the relevant T_e and N_e), dereddened Hβ fluxes and CEL diagnostic physical parameters of the four regions are listed in Table 2. Lists of the identified lines, observed and dereddened line fluxes for the four region spectra are provided in Appendix E.

The diagnostics of the four regions listed in Table 2 confirm at higher S/N the trends shown in Figs. 5 and 6 for T_e and N_e at higher and lower ionization respectively, and the radial profiles in Fig. 7. Most notable was the increase in T_e at the outer edge of the core from about 8500 K (from both [S III] and [N II]) to 11 000 K and the decrease in N_e from ~2500 to 650 cm^{-3} (mean from [Cl III] and [S II]). The halo must also have a lower filling factor since the decrease in N_e^2 between the core and halo is ~20× less than the drop in surface brightness.

The difference in the T_e and N_e values between the values in Table 2 and the images (and the radial profiles) can be understood both in terms of S/N and weighting by the line fluxes contributing to the diagnostic ratios. Taking [N II] T_e as an example, for the area of the four regions, the mean unweighted spaxel values are (Core, Low c, Halo, Total) 8660, 9510, 11 100, 10 550 K, to be compared with those in Table 2, col. 9. The largest difference in diagnostics between integrated and spaxel-by-spaxel average values is for the Total nebula area, where the flux weighting by the spaxels of the bright core lower the integrated value in comparison to the areal mean of T_e values.

The increase in T_e from the rather uniform value in the core to the higher but also uniform value in the halo occurs over a rather narrow range of 6–9″ offset, precisely where N_e begins to decrease beyond 6″ radius into the halo. As the radial profiles demonstrate (Fig. 7), it is in this range where the extinction also decreases. The images of [O III] emission (Fig. 2, upper right) show that some higher ionization emission escapes from the denser core into the surroundings, so the core is not entirely optically thick to photons with energies >35 eV; the lower density of O^{++} can lead to reduced cooling, hence a hotter halo. Also the effect of radiation hardening, whereby the frequency dependence of the H photoionization cross section above 13.6 eV permits the larger fraction of higher frequency photons to produce a hotter halo. Sandin et al. (2008) observed a hotter halo than core (from [O III] T_e measurements) in some PNe (NGC 6826, NGC 7662 and IC 3568) as did Monreal-Ibero et al. (2005) for NGC 3242.

[4] In the UVES spectrum, the He I 4471 Å line has a blue wing, extending to −300 km s^{-1} from the absorption line centre. In the much lower resolution Anglo-Australian Telescope (AAT) spectrum, the stellar absorption line was completely filled in by nebular emission.

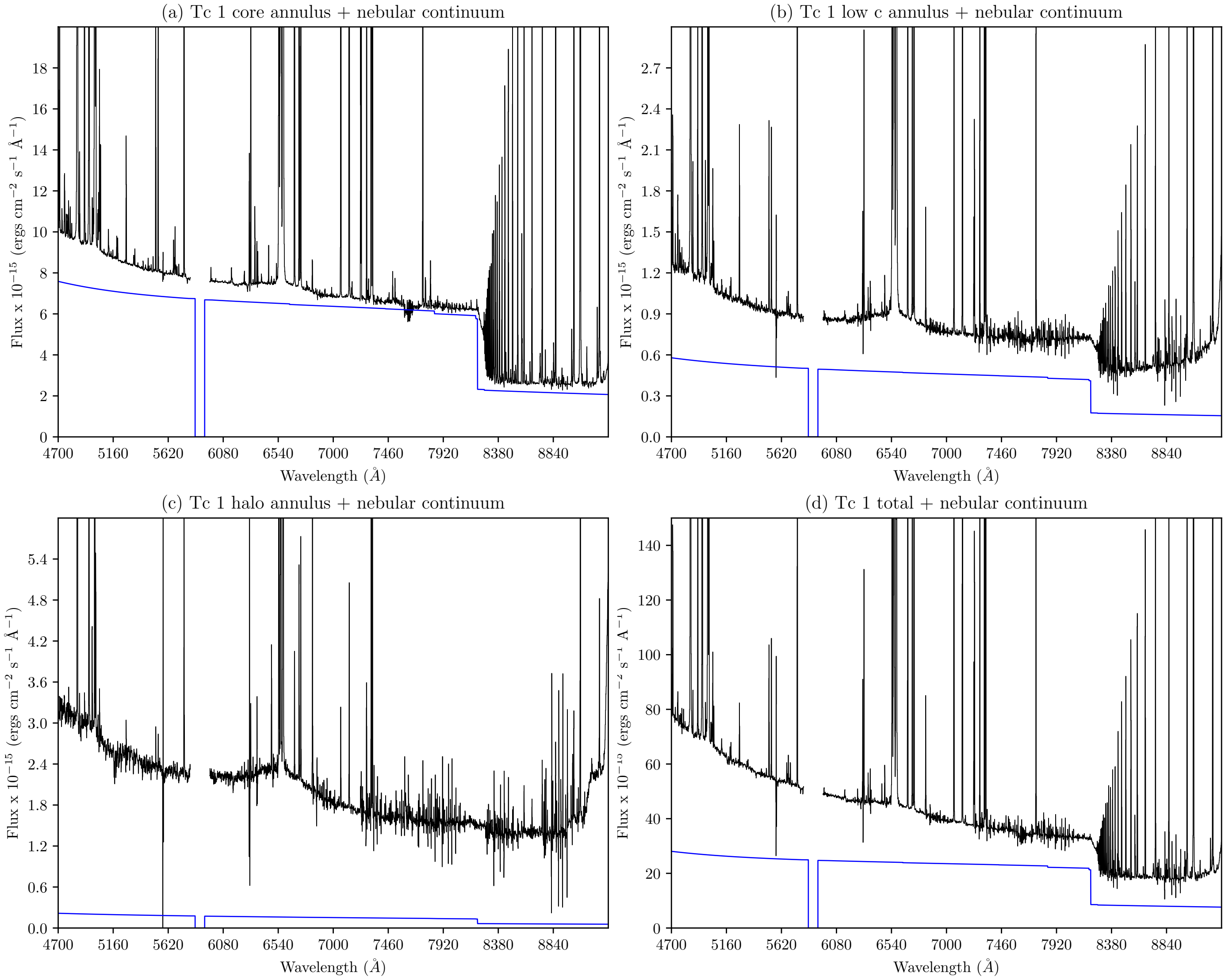

Fig. 12. Dereddened spectra of the four summed regions: (a) bright core annulus; (b) annulus of low c(Hβ) spaxels; (c) halo annulus; and (d) total nebula. The dereddened spectra are shown in black and the fitted nebular continuum (sum of H^+ b-f, f-f and 2-photon and He^+ b-f) in blue. The spectra highlight the continuum shape and level for the four spectra with the majority of the emission line peaks off scale. See text for further details for the four regions and Table 3 for inputs to the nebular continuum calculations.

Both studies found increases in T_e up to ∼4000 K, larger than 2500 K observed here for Tc 1. The MUSE observations provide sufficient 2D data for a detailed photoionization model of Tc 1, so that the radiation transfer between core and halo could be studied.

5.4.2. Continuum emission

Figure 12 shows the four spectra, plotted in $\log_{10}$ flux and focussing on the continuum. For the inner nebula annulus, the continuum is strong and the Paschen jump at ∼8205 Å can be used as a T_e indicator; for the low extinction annulus, the continuum is weaker but shows a Paschen jump, continuum generally increasing bluewards and an abrupt increase in flux redwards of ∼8900 Å; the halo continuum is very weak with a discernible Paschen jump but similar blue slope and rise in the far red. We attribute the rise in flux at $\lambda \gtrsim 8500$ Å to 2nd order contamination from the MUSE Volume Phase Holographic Grating of light at $\lambda \lesssim 4700$ Å (and an effect of defocus of the 2nd order for some slices), as documented in the MUSE instrument manual[5]. Given that these aperture spectra are sums of many spaxels (IFUs and slicers), then the fractional effect is noticeable, particularly where the red continuum is low (as in the two outer annuli). It was assumed that the bright CSt is the origin of this 2nd order continuum (since the MUSE PSF in the far red has significant 'arms' in the cardinal directions), but there may also be a contribution from the blue nebular continuum ($\lambda < 4700$ Å) from the bright core. As this 2nd order contamination of the spectra is explained as a purely instrumental effect, it will not be further mentioned in an astrophysical context.

In order to determine the strength and spectral shape of any continuum in excess of the atomic nebular continuum, in each of the observed spectra the atomic nebular continuum (sum of b-f, free-free [f-f] and 2-photon for H^+ and He^+) was calculated and subtracted. This analysis requires the spectra to be dereddened (using the extinction derived from the observed Hα/Hβ

[5] https://www.eso.org/sci/facilities/paranal/instruments/muse/doc.html

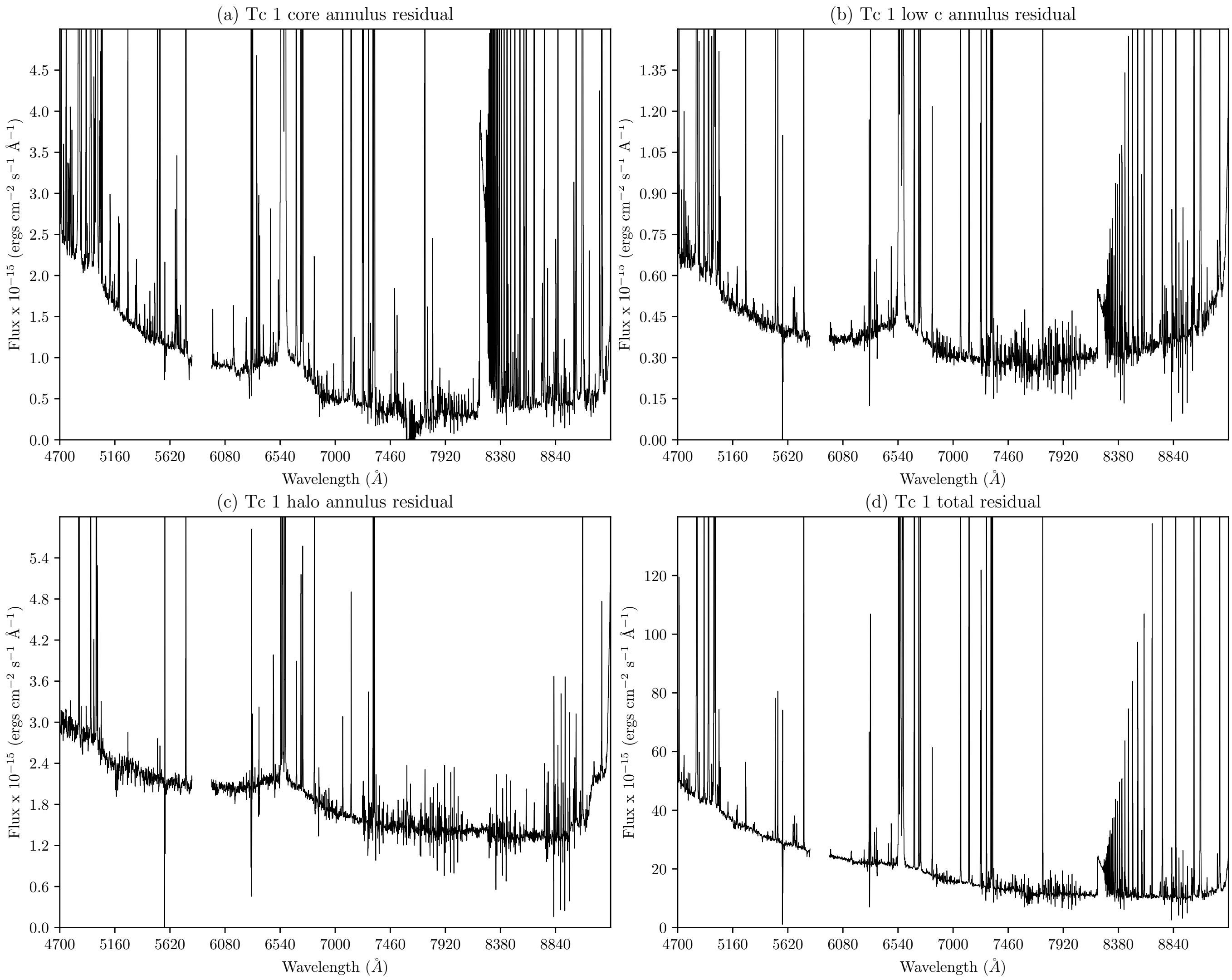

Fig. 13. Residual spectra of the dereddened spectrum of the four summed regions (reddened spectra in Fig. 12) with the nebular continuum (see Fig. 12) subtracted: (a) bright core annulus; (b) annulus of low c(Hβ) spaxels; (c) halo annulus; and (d) total nebula. See Table 3 for inputs to the nebular continuum calculations.

compared to Case B for the appropriate T_e and N_e), the dereddened Hβ flux and the He$^+$/H$^+$ number ratio; compare (Walsh et al. 2018, Appendix A). Here the results for the nebular continuum were calculated in the dipso spectral analysis package (Howarth et al. 2014). Table 3 lists the basic parameters of the nebular continuum fits and Fig. 13 shows the results of subtracting the nebular continuum from each annulus spectrum. The T_e values were not calculated from the size of the Paschen jump (e.g. Zhang et al. (2004), Walsh et al. (2018)), but instead the values from the CEL ratios were used (see footnote to Table 3).

All four residual spectra with the nebular continuum subtracted in Fig. 13 show a continuum over all wavelengths with an increase to the blue. We consider a number of explanations for this extra continuum:

1. Scattered continuum. The increase to the blue is steepest for the annulus over the nebula that is closer to the CSt. Thus the source could be instrument scattered light from the CSt with some addition of intra-nebular scattered light. The level of the residual blue continuum (mean over 4750–4850 Å), is 8.0×10^{-17} erg cm^{-2} s^{-1} Å^{-1} arcsec^{-2}) for the mean offset of 4.4″ of the nebular annulus from the CSt; when compared to the dereddened stellar continuum (Sect. 5.3 and Fig. 11) over the same wavelength range, the ratio is 2.4×10^{-4} ″$^{-2}$. However for the low c annulus, the shape of the continuum is less blue than that of the dereddened CSt, tending to rule out scattering within the nebula of the starlight (where typical ISM dust produces a blueing of the spectrum) in this region. The reddened residual continuum (i.e. the residual spectrum of the dereddened continuum minus the nebular continuum, then reddened by the line of sight extinction) can also be compared to the observed CSt spectrum and is a probe of instrumental scattering. For the core annulus, the reddened residual also shows a contribution increasing to the blue, (neglecting the 2nd order contamination above ~8500 Å) relative to the CSt spectrum, but not so for the low c or outer annuli with larger offsets.

These comparisons of continuum slope in the spectra of the two inner annuli with that of the CSt, are consistent with a decreasing level of scattering with offset from the CSt. For the outer annulus located over the halo (mean offset 2.1× that of the core annulus) however, the residual was redder than the CSt spectrum. Here the contamination in this

aperture from field stars was considerable (estimated at 55% at 5500 Å by removing all the star images from the annulus region in the v' image (Fig. 3) and these tend to be red (cf. the star colours in Table A.1 with those of the CSt, $b' - v'$ −0.39, $v' - r'$ −0.45, $v' - i'$ −1.43).
2. Enhanced nebular continuum. Enhanced 2-photon continuum has been observed in shock excited Herbig–Haro objects (Dopita et al. 1982), so a possible origin to the residual continuum could be an increase of 2-photon continuum over that predicted. However the residual continuum is flatter than a 2-photon continuum for all four regions, refuting this suggestion.
3. Instrumental scattering. For the total spectrum of Tc 1 with the nebular continuum subtracted, the residual continuum is blue and this has also been seen in the total spectra of other PNe observed with MUSE – for NGC 4361 (Walsh et al. 2024), their Fig. 9, and from analysis of the total spectrum of NGC 7009 (Walsh et al. 2018). Comparing the shapes of the residual continuum for the total flux in the MUSE field of view (excluding the CSt) between the three nebulae shows good agreement in spectral shape between NGC 4361 and Tc 1, whilst for NGC 7009 there is a divergent broad feature under the Hβ and [O III] 4959 and 5007 Å lines extending to ~5500 Å, probably arising from the wings of the grating line spread function around the very strong emission lines. This comparison is detailed in Appendix D and emphasises the striking similarity in the shape of the residual continua of these three PNe observed with MUSE.

The most likely explanation for the excess continuum would appear to be in terms of instrument scattered light within the MUSE optics. Presumably the total continuum (sum of starlight and nebular continuum, faint wings of the grating line profile around the strong Hβ, Hα and [O III] lines, and perhaps also integrated line emission) supplies the scattered light. In Appendix D, a comparison of the residual continuum after nebular continuum subtraction in the three MUSE datasets (NGC 7009, NGC 4361 and Tc 1), which were analysed for these effects, is presented.

One feature of the spectrum of the Tc 1 annuli that distinguishes them was the broad wing around Hα, extending over ~500 Å, which appears to be present in all three annulus spectra, and the total spectrum, but not detectable at Hβ. This broad profile is symmetric about the approximate observed wavelength of Hα of FWHM ~380 Å. The broad profile is 12 times stronger relative to the flux in Hα in the outer annulus than the low-c annulus, and 50 times lower for the core annulus (where the line emission is highest). This broad emission is present in all areas of the nebula but strongest in surface brightness in the core, consistent with a scattering origin from the centrally peaked (~3.2″ diameter) high emission surface brightness region. Aleman et al. (2019) also remark on broad components to the bright lines, but only over FWHM extents of ~1000 km s^{-1}, and these may be the low intensity wings of the grating line profile. The origin of the broad feature is unclear: the electron density is quite low so electron scattering seems an unlikely origin.

5.5. Critical further observations

Tc 1 is distinguished, in particular, from other PNe mapped in 2D by the two features revealed from these comprehensive optical IFU observations: the low c(Hβ) annulus around the core and the halo of enhanced 7281 Å emission above that expected for He I. Other spectroscopic observations would be very helpful to conclusively determine if scattering effects within the MUSE instrument were not responsible for these results. Scattering effects are explicitly considered in Appendix B in the case of the low c annulus, but for the 7281 Å excess it was difficult to understand why only this line should be more prone to scattering than the nearby He I 6678 Å line. For example, longer slit observations at several positions across the core-halo region, with and without inclusion of the CSt in the slit, could independently confirm these results. In addition higher spectral resolution would be an advantage, to determine if any velocity shifts, or complex emission line profiles occur in the core-to-halo transition region. Also imaging and spectroscopy in the infrared, as performed by Cami et al. (in prep.) with JWST, can study the dust emission distribution to determine if the low c annulus represents a deficiency of dust, or a spatial change in dust grain properties.

6. Conclusions

Deep MUSE wide field observations of the fullerene emitting PN, Tc 1, have been presented for the optical range 4700–9300 Å. Tc 1 has been has been shown to be in most respects a typical PN in its early phase of transition from the AGB to white dwarf, with modest ionization, a rather symmetric structure and a central star with an effective temperature between 31 000 K and 34 000 K (see discussion in Sect. 5.3.2). Its core is larger (full diameter 0.21 pc) than would be expected for a younger PN and its dynamical time (Sect. 5.1) is longer than for the 2M$_\odot$ mass evolutionary track suggested by the (T_{eff}, L) value (Sect. 5.3). The filamentary halo is extended (56″, 0.96 pc) with a long dynamical time (Sect. 5.1) and may be the remnant of the AGB wind. MUSE data cubes at three exposure levels were analysed to provide combined unsaturated images in emission lines covering the range of surface brightness from Hα to faint lines (< 10^{-3} Hβ). These optical observations are highly complementary to recent JWST mid-infrared imaging spectroscopy with MIRI and NIR imaging with NIRSPEC (Cami et al., in prep.; Schuylenberg et al., in prep.).

Emission line images extracted from the datacubes were presented. The spectra of 33 field stars over the area of the faint halo affected the extinction determination from Hα/Hβ. Template spectra were fitted to these stars to subtract their spectra and improve the fidelity of local extinction determination. Collisionally excited line diagnostics for T_e and N_e were imaged; optical recombination line diagnostics for Paschen Jump T_e and He I T_e were also presented.

Three main morphological features of Tc 1 emerge from this study: the bright core, a periphery with lower surface brightness surrounded by the faint halo. The core shows a 2″ elliptical ring around the CSt and groups of brighter knots of lower ionization to the NW and SE. These knots have been shown by Bouvis et al. (2025) to be similar to LIS found in other PNe and now revealed to have offset velocities from the systemic (Sect. 5.1). The transition region between core and halo has lower N_e than in the core, and also higher T_e, the latter probably on account of radiation hardening, and also shows two remarkable properties: a ring of lower extinction, which, when corrected by the larger scale interstellar extinction, implies negative extinction for a standard reddening law. In this region also the T_e sensitive He I 7281/6678 Å ratio shows an increase above the maximum value allowed from radiative transfer: the presence of a contaminating line was investigated, but no convincing candidate species could be established. The origin of this anomalous He I line ratio therefore remains unanswered from these observations.

In order to confirm the results from the spaxel images, four integrated regions (core, low c annulus, halo and total nebula), were defined and diagnostics from their high S/N spectra were analysed. These spectra allowed detailed examination of the continuum and in all cases an excess above the nebular continuum (b-f, f-f and 2-photon) was found. This effect has also been seen in previous MUSE spectra of PNe with bright central stars and instrumental scattering of starlight was suspected. However the shape of the excess continuum does not match the CSt spectral shape. The spectrum of the bright CSt of Tc 1 was extracted from the cubes and then dereddened over the 4700–9300 Å range using different values of c(Hβ). Each of the dereddened continua was compared with LTE model atmospheres with differing effective temperatures and surface gravities. It was found that a CSt extinction of c(Hβ) = 0.385 and an LTE model with $T_{\rm eff}$ = 31 000 K and log g = 3.5 minimized the differences between the continuum slopes of the dereddened central star and the model atmospheres. This effective temperature was within the range found by other investigators, while the deduced extinction towards the CSt is consistent with the increase in reddening towards the centre that was found in the extinction map (Fig. 4).

Given that the annulus of low c values occurs just outside the bright core where the nebular surface brightness decreases rapidly, an effect of the point spread function on extinction determination could be suspected and an investigation with image restoration at Hβ and Hα wavelengths was performed. While a small effect on the extinction could be induced, the depth of the low c annulus could not be reached, leaving the conclusion that this was a real effect. Two suggestions for this strong spatial change in c(Hβ) were discussed: scattering by small dust grains in the nebula causing 'blueing' of the spectrum, hence inducing increased Hβ/Hα ratios; or a local change of the ratio of total to selective extinction, R_V, of the dust in this region. The former was investigated by a simple 3D dust scattering model and at least a part of the drop in c(Hβ) could be thus explained. The latter effect, an increase in R_V due to an increase in mean grain size, would appear to be the more promising in order to explain the apparent drop in c(Hβ) in the low c annulus. The decline in c(Hβ) values occurs just beyond the peak of the fullerene C_{60} emission rim studied by JWST MIRI spectra (Geise et al., in prep.), which suggests a possible connection between the dust extinction and fullerene emission. A change in the dust grain properties in the vicinity of the fullerene peak should be further investigated, such as through ultra-violet and near-infrared spectra to determine the nature of the local reddening law or high spectral resolution observations to determine effects of an unusual velocity field or the presence of shocks.

MUSE again reveals the complexity of the extinction in a PN (cf. NGC 7009, Walsh et al. 2018), here complicated by the annulus of low c values. Given that c(Hβ) measures the line-of-sight extinction integrated along the column of emission, and is partly dependent on the emission distribution, the true dust structure is likely to be more complex than the image (Fig. 4) suggests. Further optical – infrared observations are required to better understand the unusual features of Tc 1 revealed in this study and if they are indicative of the presence of fullerenes.

Data availability

The reduced MUSE datacubes at the three exposure levels (40, 101 and 595 s) will be made publicly available through the ESO Science Archive via the Phase 3 process. Tables 1, A1, E1, E2, E3, and E4 are available at the CDS via `https://cdsarc.cds.unistra.fr/viz-bin/cat/J/A+A/713/A103`.

Acknowledgements. Based on observations collected at the European Southern Observatory under ESO programme 105.20R7.001. We thank the VLT observing support team and telescope operators for enabling these fine observations. We are grateful for discussions with Peter Weilbacher and Roland Bacon on the possible origin of the residual continuum in the spectra of several PNe, as described in Appendix D. We thank the referee, Joel Kastner, for his discerning comments that led to a sharpening of focus of the paper. JC and EP acknowledge support from an NSERC Discovery Grant. This research has made use of NASA's Astrophysics Data System Bibliographic Services. This work has made use of data from the European Space Agency (ESA) mission *Gaia* (`https://www.cosmos.esa.int/gaia`), processed by the *Gaia* Data Processing and Analysis Consortium (DPAC, `https://www.cosmos.esa.int/web/gaia/dpac/consortium`). Funding for the DPAC has been provided by national institutions, in particular the institutions participating in the Gaia Multilateral Agreement. This research has greatly benefited from the use of PyNeb (Luridiana et al. 2015), for the nebular diagnostics. We are grateful to the communities who have developed the Python packages used in this research, such as MPDAF (Piqueras et al. 2019), Astropy (Astropy Collaboration 2013, 2018, 2022), numpy (Walt et al. 2011), scipy (Jones et al. 2001) and matplotlib (Hunter 2007).

References

Abdurro'uf, Accetta, K., Aerts, C., et al. 2022, ApJS, 259, 35
Aleman, I., Leal-Ferreira, M. L., Cami, J., et al. 2019, MNRAS, 490, 2475
Astropy Collaboration (Robitaille, T. P., et al.) 2013, A&A, 558, A33
Astropy Collaboration (Price-Whelan, A. M., et al.) 2018, AJ, 156, 123
Astropy Collaboration (Price-Whelan, A. M., et al.) 2022, ApJ, 935, 167
Bacon, R., Accardo, M., Adjali, L., et al. 2010, Proc. SPIE, 7735, 773508
Bacon, R., Vernet, J., Borisova, E., et al. 2014, The Messenger, 157, 13
Berné, O., Cox, N. L. J., Mulas, G., & Joblin, C. 2017, A&A, 605, L1
Bouvis, K., Akras, S., Monteiro, H., et al. 2025, A&A, 700, A155
Cami, J., Bernard-Salas, J., Peeters, E., & Malek, S. E. 2010, Science, 329, 1180
Cardelli, J. A., Clayton, G. C., & Mathis, J. S. 1989, ApJ, 345, 245
Castelli, F., & Kurucz, R. L. 2004, New Grids of ATLAS9 Model Atmospheres
Chornay, N., & Walton, N. A. 2021, A&A, 656, A110
Conti, P. S., & Alschuler, W. R. 1971, ApJ, 170, 325
Corradi, R. L. M., Schönberner, D., Steffen, M., & Perinotto, M. 2003, MNRAS, 340, 417
Datta, D., & Kumar, S. 2009, J. Appl. Phys., 106, 074517
Díaz-Luis, J. J., García-Hernández, D. A., Kameswara Rao, N., Manchado, A., & Cataldo, F. 2015, A&A, 573, A97
Dopita, M. A., Binette, L., & Schwartz, R. D. 1982, ApJ, 261, 183
Draine, B. T. 2011, Physics of the Interstellar and Intergalactic Medium
Fang, X., & Liu, X.-W. 2011, MNRAS, 415, 181
Ferland, G. J., Chatzikos, M., Guzmán, F., et al. 2017, Rev. Mexicana Astron. Astrofis., 53, 385
Fétick, R. J. L., Fusco, T., Neichel, B., et al. 2019, A&A, 628, A99
Fried, D. L. 1966, J. Opt. Soc. Am., 56, 1372
García-Hernández, D. A., Villaver, E., García-Lario, P., et al. 2012, ApJ, 760, 107
Gielen, C., Cami, J., Bouwman, J., Peeters, E., & Min, M. 2011, A&A, 536, A54
Howarth, I. D. 1983, MNRAS, 203, 301
Howarth, I. D., Murray, J., Mills, D., & Berry, D. S. 2014, DIPSO: Spectrum analysis code, Astrophysics Source Code Library [record ascl:1405.016]
Hunter, J. D. 2007, Comput. Sci. Eng., 9, 90
Jones, A. P., Tielens, A. G. G. M., Hollenbach, D. J., & McKee, C. F. 1994, ApJ, 433, 797
Jones, E., Oliphant, T., Peterson, P., et al. 2001, SciPy: Open source scientific tools for Python
Kingdon, J., & Ferland, G. J. 1995, ApJ, 442, 714
Kirchschlager, F., Schmidt, F. D., Barlow, M. J., et al. 2019, MNRAS, 489, 4465
Knapp, G. R., Young, K., Lee, E., & Jorissen, A. 1998, ApJS, 117, 209
Lindegren, L., Klioner, S. A., Hernández, J., et al. 2021, A&A, 649, A2
Lucy, L. B. 1974, AJ, 79, 745
Luridiana, V., Morisset, C., & Shaw, R. A. 2015, A&A, 573, A42
Marigo, P., Bernard-Salas, J., Pottasch, S. R., Tielens, A. G. G. M., & Wesselius, P. R. 2003, A&A, 409, 619
Martins, F. 2018, A&A, 616, A135
Massey, P., Puls, J., Pauldrach, A. W. A., et al. 2005, ApJ, 627, 477
Mathis, J. S., Rumpl, W., & Nordsieck, K. H. 1977, ApJ, 217, 425
Menzel, D. H., & Baker, J. G. 1937, ApJ, 86, 70
Miller Bertolami, M. M. 2016, A&A, 588, A25
Moehler, S., Modigliani, A., Freudling, W., et al. 2014, A&A, 568, A9
Moffat, A. F. J. 1969, A&A, 3, 455
Monreal-Ibero, A., Roth, M. M., Schönberner, D., Steffen, M., & Böhm, P. 2005, ApJ, 628, L139

Otsuka, M. 2019, MNRAS, 482, 2354
Otsuka, M., Kemper, F., Cami, J., Peeters, E., & Bernard-Salas, J. 2014, MNRAS, 437, 2577
Pauldrach, A. W. A., Hoffmann, T. L., & Méndez, R. H. 2004, A&A, 419, 1111
Peimbert, M. 1971, Bol. Observ. Tonantzintla Tacubaya, 6, 29
Piqueras, L., Conseil, S., Shepherd, M., et al. 2019, in Astronomical Society of the Pacific Conference Series, 521, Astronomical Data Analysis Software and Systems XXVI, eds. M. Molinaro, K. Shortridge, & F. Pasian, 545
Porter, R. L., Ferland, G. J., Storey, P. J., & Detisch, M. J. 2012, MNRAS, 425, L28
Porter, R. L., Ferland, G. J., Storey, P. J., & Detisch, M. J. 2013, MNRAS, 433, L89
Pottasch, S. R., Surendiranath, R., & Bernard-Salas, J. 2011, A&A, 531, A23
Pruijt, B. G. A., Monreal-Ibero, A., Weilbacher, P. M., et al. 2026, MNRAS, 549, stag794
Ren, S. L., Wang, Y., M., R. A., et al. 1991, Appl. Phys. Lett., 59, 2678
Richardson, W. H. 1972, J. Opt. Soc. Am., 62, 55
Rogers, C., Brandl, B., & De Marchi, G. 2024, A&A, 688, A111
Rouleau, F., & Martin, P. G. 1991, ApJ, 377, 526
Rubin, R. H., Simpson, J. P., O'Dell, C. R., et al. 2011, MNRAS, 410, 1320
Sandin, C., Schönberner, D., Roth, M. M., et al. 2008, A&A, 486, 545
Schlegel, D. J., Finkbeiner, D. P., & Davis, M. 1998, ApJ, 500, 525
Schwarz, H. E., Corradi, R. L. M., & Melnick, J. 1992, A&AS, 96, 23
Sellgren, K., Werner, M. W., Ingalls, J. G., et al. 2010, ApJ, 722, L54
Sharpee, B., Williams, R., Baldwin, J. A., & van Hoof, P. A. M. 2003, ApJS, 149, 157
Ströbele, S., La Penna, P., Arsenault, R., et al. 2012, SPIE Conf. Ser., 8447, 844737
Stuik, R., Bacon, R., Conzelmann, R., et al. 2006, New A Rev., 49, 618
Thackeray, A. D. 1950, MNRAS, 110, 524
Ueta, T., Ladjal, D., Exter, K. M., et al. 2014, A&A, 565, A36
van de Hulst, H. C. 1981, Light scattering by small particles
van Hoof, P. A. M. 2018, Galaxies, 6, 63
Vergely, J. L., Lallement, R., & Cox, N. L. J. 2022, A&A, 664, A174
Vernet, J., Dekker, H., D'Odorico, S., et al. 2011, A&A, 536, A105
Vogt, F. P. A., Bonaccini Calia, D., Hackenberg, W., et al. 2017, Phys. Rev. X, 7, 021044
Walsh, J. R., Monreal Ibero, A., Laging, J., & Romeijnders, M. 2024, A&A, 690, A264
Walsh, J. R., Monreal-Ibero, A., Barlow, M. J., et al. 2016, A&A, 588, A106
Walsh, J. R., Monreal-Ibero, A., Barlow, M. J., et al. 2018, A&A, 620, A169
Walt, S. v. d., Colbert, S. C., & Varoquaux, G. 2011, Comput. Sci. Eng., 13, 22
Weilbacher, P. M., Streicher, O., Urrutia, T., et al. 2014, in Astronomical Society of the Pacific Conference Series, 485, Astronomical Data Analysis Software and Systems XXIII, eds. N. Manset, & P. Forshay, 451
Weilbacher, P. M., Palsa, R., Streicher, O., et al. 2020, A&A, 641, A28
Williams, R., Jenkins, E. B., Baldwin, J. A., et al. 2008, ApJ, 677, 1100
Yan, R., Chen, Y., Lazarz, D., et al. 2019, ApJ, 883, 175
Zhang, Y., Liu, X.-W., Wesson, R., et al. 2004, MNRAS, 351, 935
Zhang, Y., Liu, X.-W., Liu, Y., & Rubin, R. H. 2005, MNRAS, 358, 457

Appendix A: Procedure for fitting continuum of field stars

Given the complexity of the spectra of the generally late-type field stars, and the dangers in fitting high order functions to the continuum in order to measure the emission line fluxes, it was decided to use spectra of observed stars. The requirements are a library of spectra covering a wide range of spectral types well-sampled by sub-type, and at a spectral resolution, higher or close to that of MUSE. The SDSS-IV MaStar spectral library (Yan et al. 2019) was selected as the most appropriate, being large and based on observed spectra rather than a model library. The spectral coverage (3622–10354 Å) is wider than MUSE, the resolution at R∼ 1800 close to that of MUSE; the library is extensive with a broad range of spectral types; the 1st release with 3321 star spectra was employed. The full MaStar release (24130 stars) is described in Abdurro'uf et al. (2022), but only the first release was used in this work.

The magnitudes of the stars in the MaStar database were determined in four filters, chosen carefully to avoid stronger emission lines so that the comparison to magnitudes of stars on the MUSE cube would be minimally biased by the presence of emission. The intermediate width, square profile, filter bands were: b' 4712.5–4850.0 Å; v' 5400–5600 Å; r' 6320–6520 Å; and i' 7900–8100 Å. Then the colours ($b'-v'$, $v'-r'$, $v'-i'$) of the field stars in the MUSE field over the area of the halo were compared to the same set of synthetic magnitudes for all the stars in the MaSTar database in order to select a MaStar star, or stars, matching as closely as possible in spectral shape to the observed stars. 29 stars were identified in the halo as influencing the determination of c(Hβ) from comparison of Hα/Hβ to the Case B value; they are indicated on Fig. 3. The magnitudes of these stars were measured by simple aperture photometry using IRAF *imexam* (photometric aperture 0.6″ radius with a background annulus 1.2–1.8″). Comparing the v' magnitude of the brightest field stars with the Gaia G magnitude and correcting to Johnson V magnitude using the colour terms from Carrasco (2021)[6] enabled the indicative V' mags of the stars to be estimated (neglecting colour terms and extinction). The positions of these stars, relative to the position of the CSt, their V' mags and the ($b'-v'$), ($v'-r'$), ($v'-i'$) colours are listed in Table A.1; these stars range over $\Delta\ V'$ of 4.2 mags.[7]

The closest sets of matches to the ($b'-v'$), ($v'-r'$) and ($v'-i'$) colours of the field stars were selected from the MaStar database and the spectra retrieved. For an oversized area around each field star in Table A.1 (typically 100 spaxels but depending on the brightness of the star), a MaStar spectrum was separately scaled to the continuum on both sides of the Hα and Hβ lines for each spaxel and subtracted from the observed spectrum. The resulting absorption line subtracted spectrum was then refitted by a Gaussian and the revised Hα or Hβ line flux inserted into the flux map. This process required considerable oversight, as the indicative spectra from the colour matches often did not clearly match the obvious Hβ and Hα absorption line shape and depth, and in some cases only one of Hα or Hβ would match well for a given MaStar spectrum. In these cases fits by stars with similar ($b'-v'$), ($v'-r'$) and ($v'-i'$) colours were trialed until a better match to the absorption line shape around the Hα or Hβ emission lines was found. This procedure could be automated but it is clear that many spectra may be required to locate a good match and a minimization algorithm would be needed to find 'best' matches (of course within the limits of the available spectra in the database and differences in reddening for the database star and the observed field star).

Applying this correction procedure for the effect of field star spectra, most of the apparent emission or absorption features in the Hβ and Hα images were removed so that no excursions in extinction from the local mean were observed at these positions. Since the field star absorption around Hα could sometimes be broad, the [N II] 6548, 6583 Å and [S II] 6716, 6731 Å lines were also refitted in the corrected spectra; however this step was only found necessary for the set of 595 s exposures, as the effect of the star continuum fit for the shorter exposures was not significant for the line flux images.

Table A.1. Position and photometry of interfering field stars

Star	$\Delta\ \alpha$ (″)	$\Delta\ \delta$ (″)	V′ mag.	($b'-v'$) mag.	($v'-r'$) mag.	($v'-i'$) mag.
1	5.9	-18.3	16.37	0.00	-0.08	-0.37
2	21.7	-3.1	17.43	0.01	-0.07	-0.34
3	23.1	17.4	16.28	0.05	-0.04	-0.28
4	18.8	14.5	19.89	0.01	-0.08	-0.33
5	25.1	8.1	17.65	1.52	-1.59	-1.82
6	6.0	26.0	18.42	-0.41	0.57	0.53
7	6.1	27.1	17.85	0.19	-0.03	-0.10
8	-8.1	23.7	17.66	0.10	0.00	-0.16
9	8.4	3.0	17.10	0.03	-0.09	-0.32
10	15.2	23.0	19.10	0.09	-0.05	-0.24

Notes. Column 4 lists the V' mag., corrected from the measured 5400–5600 Å narrow band magnitude by the G mag. of several stars from Gaia; see text for details.
Only the first ten entries of this table are shown; the full table is available in electronic form at the CDS.

Appendix B: Reality of the extinction structure – Image restoration

In order to obtain accurate quantitative images of the nebula at different wavelengths with the observed PSF deconvolved, a high fidelity PSF sampled at those wavelengths is required. This is feasible with a grid of well-exposed and separated stars taken in the same field (or possibly an adjacent field immediately pre- or post-ceding the nebula target exposures), but the available set of images of Tc 1 could not achieve this goal. Models of the MUSE PSF (as parameters of a Moffat (Moffat 1969) profile) can be made using the *psfr* task (Fétick et al. 2019) based on the seeing and AO parameters of an exposure read from the image header. However given that the MUSE cubes were formed from multiple exposures, all with differing atmospheric and AO settings, a combined model of the PSF is required.

The closest fidelity to an image-based PSF is to use a selected star, or stars, in the image of interest, such as shown in Fig. 3. The brightest star is the CSt itself, but lies on a field of bright structured emission, so even when selecting narrow wavelength ranges away from bright emission lines, the nebular continuum

[6] Carrasco (2021): https://gea.esac.esa.int/archive/documentation/GDR2/Data_processing/chap_cu5pho/sec_cu5pho_calibr/ssec_cu5pho_PhotTransf.html

[7] A further field star was found projected on the bright core (offsets $\Delta\alpha$+2.4, $\Delta\delta$+3.5 ″) when estimating the contribution of all field stars to the continuum for the aperture over the halo (see Sect. 5.4). In the V' band this star had an estimated mag. of 19.7, and contributed only 17% to the local V' surface brightness. Its effect on emission line measurements was not detectable and no feature was seen in the c(Hβ) extinction image (see Sect. 4.1 and Figure 4) at this position.

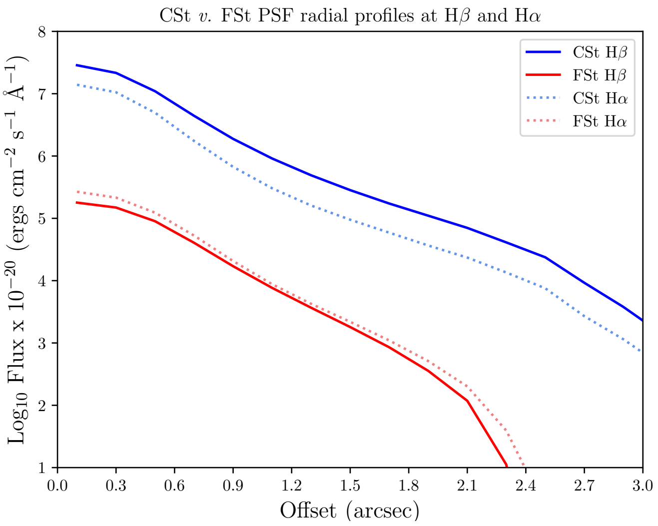

Fig. B.1. Radially averaged profiles of the observed point spread functions for the central star (CSt, blue lines) and the field star, X (FSt, red lines), at Hβ (continuous lines) and Hα (dotted lines). Log_{10} flux (spaxel^{-1}) is plotted against offset from the centre of the peak spaxel.

and faint lines are always present. Choice of a suitable field star is limited by the nebular extent. The brightest field star (coincidentally not situated on the nebula halo) is the one marked X in Fig. 3 with V mag 14.4 (see Table A.1). However this star is situated close to the field edge so the PSF wings cannot be sampled to large radii. Clearly any deconvolution will be subject to uncertainties, in addition to the typical ringing around point sources and noise amplification induced by Fourier or iterative deconvolution methods. Thus we set a modest goal of trying to determine if the extinction deficit in an annulus around the bright core could be returned to a value close to that for the halo (and of the ISM) by restoring Hα and Hβ images and examining their ratio on the restored images.

PSFs for the field star X and the CSt were made by extracting images from the 40 s cube (on the 101 and 595 s cubes the CSt is saturated) at wavelengths bluewards and redwards of each line (for Hβ: 4820–4850 and 4870–4900 Å; and for Hα: 6515–6545 and 6585–6615 Å avoiding the [N II] 6548, 6583 Å lines) and averaging the pairs to form single Hβ and Hα PSFs. In the case of the PSF for the CSt, an attempt was made to remove the nebula contribution by subtracting a scaled version of the emission line map matched in mean level to the extended emission; however the attempt did not result in far PSF wings with mean zero signal, probably on account of the local structure of the ionized emission. Fig. B.1 show the radially averaged PSFs of the CSt (blue lines) and the field star X (red lines) demonstrating the large wings to the CSt and the curtailed wings to the (fainter) field star (also on account of its proximity to the image edge). The CSt and field star PSFs show similar shape at the same wavelength to 2.0″ radius offset but for Hα the CSt has a notably narrower PSF than at Hβ, dissimilar to the field star. 2D Gaussian and Moffat fits to these stars are listed in Table B.1.

These PSF images were used to restore the Hβ and Hα emission line images using Richardson-Lucy (Richardson (1972), Lucy (1974)) iterative restoration[8]. Since the deconvolved PSFs did not have the same width on the Hβ and Hα restored images, then after the iterative restoration the images were convolved with a two-dimensional Gaussian of the same width (FWHM 0.6″, or three pixels) before forming the Hα/Hβ ratio image. Fig. B.2 shows the comparison of the Hα/Hβ images restored from the original images employing 10 iterations with PSFs from the central star and the field star, X. A mask was applied to the noise-amplified spaxel values at the outer edge of the halo.

[8] Employing Python SciKit: skimage.restoration.richardson_lucy

Table B.1. Fits to Point Spread Function stars

H I line/ star	Gaussian FWHM (″)	Moffat α	Moffat β	Moffat FWHM(″)
Hβ				
Tc 1 CSt	0.536	0.546	3.30	0.528
Field Star X	0.568	0.524	2.78	0.558
Hα				
Tc 1 CSt	0.486	0.638	5.20	0.482
Field Star X	0.558	0.679	4.53	0.552

The Hα/Hβ ratio image restored with the CSt shows two extra rings that were not present on the original Hα/Hβ ratio image (compare the extinction map Fig. 4), and would appear to be restoration features, presumably induced by the narrow CSt Hα profile (see Fig. B.1). An alternative explanation could be that the restoration produces a thick ring of higher Hα/Hβ that is not enough to eradicate the low ratio annulus entirely. The low extinction ring was partially filled in by these two bright rings but was still visible. In contrast, for the result restored with the FSt, the low extinction ring in Hα/Hβ remains but the ratio is slightly enhanced but not by enough to remove it. The mean c(Hβ) values in a circular annulus of 1.6″ width (inner radius 6.0″) centred on the CSt showed that the image restored by the FSt produces a value only 0.01 dex. higher than the observed (*viz* unrestored) extinction map, while the mean value for the image restored by the CSt is 0.14 dex. higher. Although these experiments are not exhaustive they demonstrate that the annulus of low extinction cannot be completely removed to match the extinction value to that of the halo, arguing that it is a real feature of the nebula dust distribution. An additional test was to restore the Paschen 9 (9229 Å) image and compute the ratio to the restored Hβ image; for both restorations with CSt and FSt, the results showed that the low P09/Hβ annulus visible in the observed ratio image was not removed and indeed deepened. However the MUSE PSF was broader and had extensive structure in the wings at this long wavelength; instrument scattered light from the CSt was visible and produced bars in the cardinal directions resulting from the combination of two instrument rotations.

Appendix C: Modelling of gas+dust structure and dust extinction and scattering

A simple spherically symmetric nebula model was constructed to test how dust inside the nebula volume could affect the spatial variation of extinction and, in particular, if a shell of apparent extinction deficit could feasibly be explained. The model consists of a gas volume (producing emission) and a dust volume (responsible for extinction and scattering); the latter can be independent of the former, so not necessarily confined to fixed dust-to-gas ratio of the gaseous emission volume. Models for Hβ and Hα were constructed so that extinction maps of the model nebula could be formed for comparison with the observed extinction map (Fig. 4). Computations were performed in Python on a 200×200×200 cartesian grid.

The core nebula was simulated by a sphere with a central empty zone (radius 0.35″) and two density regimes: inner, radii 0–2.75″, density 2200 cm^{-3}; and outer, radii 3.0–6.0″, density

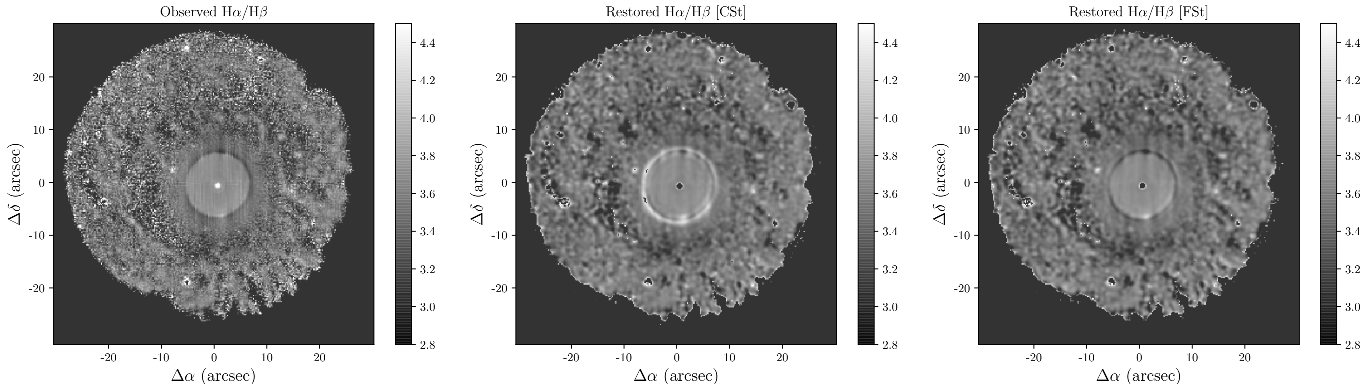

Fig. B.2. Images of the Hα/Hβ ratio of the Lucy restored Hα and Hβ images, using the central star [CSt] (centre) and the field star X [FSt] (right) as PSFs. The image of the observed Hα/Hβ ratio is shown at left. The axes display offsets with respect to the position of the CSt. For comparison, an Hα/Hβ ratio of 3.40 corresponds to c(Hβ) = 0.237 for T_e = 10 000 K and N_e = 2000 cm^{-3}.

2300 cm^{-3}, The two regimes have differing filling factors (FF), tuned to match the dereddened average Hβ surface brightness of Tc 1 from the extinction corrected 40 s cube flux map. The halo extended from radius 6.25–24.75″ with a density 700 cm^{-3} (from the nebula coadded region analysis, Sect. 5.4). The justification for a very low filling factor for the halo is apparent from the very patchy emission (Fig. 1). The quantitative details of the model components are listed in Table C.1. For each region a gas-to-dust mass (G/D) ratio was adopted, based on Ueta et al. (2014). The large scale dust was assumed to be amorphous carbon with optical constants from Rouleau & Martin (1991) and an MRN Mathis et al. (1977) size distribution ($\propto a^{-3.5}$, a_{min} = 0.005, a_{max} = 0.25) with mass density 1.8 g cm^{-3}.

Two dust shells were selectively added, an inner one (4.75–5.75″) – Dust Shell A – and an outer one (5.0–6.75″) – Dust Shell B – both with unity filling factors (see Table C.1). Dust Shell B was selected only to scatter radiation, whilst Dust Shell A could both scatter and extinguish incident and transmitted radiation. In order to explore the possibility that C_{60} could participate in the scattering of the Dust Shell B, optical constants from Datta & Kumar (2009) and Ren et al. (1991) from analysis of C_{60} thin films were employed[9] assuming the C_{60} molecule acted as a 'grain' with a size of 0.001 µm. Amplitude functions for scattered light appropriate to these particles were generated at the wavelengths of Hβ and Hα using Mie theory (e.g. van de Hulst 1981) as a function of scattering angle as tables, which were read by the Python script to model the 3D nebula. Also, the extinction cross section, C_{ext}, was computed from Mie theory at the wavelengths of Hβ and Hα for each dust species. For the amorphous carbon (AMC) MRN size distribution, all quantities of interest were integrated over the size range.

Each model was run for Case B Hβ or Hα emissivity to convert density voxels to emission flux, with the extinction produced by the line of sight dust from the emission voxel to a distant observer. Scattered emission was summed for each dust voxel taking account of the local emission, appropriately extinction corrected for the summed dust path from the emission voxel to the dust voxel; the scattered flux in the direction to the observer was also extinction corrected for its dust column. The column of voxels in the direction of the line of sight to the observer was then summed to produce maps, for example of the Hβ intrinsic and scattered emission for comparison to those observed. From the known distance, and by adjusting the filling factor (col. 6 of Table C.1), the projected emission flux could be adjusted to

[9] Adopted ($n, -k$): Hβ (1.999, 0.794); Hα (2.205, 0.796).

Table C.1. Extinction and scattering model: gas and dust volumes

Component	Inner (″)	Outer (″)	Density (cm^{-3})	G/D ratio	FF	Dust species
Core inner	0.35	2.75	2200	200	0.70	AMC
Core outer	3.00	6.00	2300	200	0.80	AMC
Halo	6.25	24.75	700	200	0.001	AMC
Dust shell A	4.75	5.75	5000	200	1.00	AMC
Dust shell B	5.00	7.00	5000	140	1.00	AMC
Dust shell C	5.00	6.75	1.0×10^8	140	1.00	C_{60}

Notes. Voxel size 0.25″, 4.28×10^{-3} pc (200^3 voxel grid);
H Balmer line emissivities calculated for T_e 9000 K, N_e = 2500 cm^{-3};
The fractional mass per H atom of 1.501 based on element abundances from Aleman et al. (2019);
The number of electrons per H atom of 1.11 was computed from the sum of the ionic abundances (Aleman et al. 2019);
AMC = amorphous carbon.

match the average values over the core and halo of Tc 1 to the dereddened images (cf. Sect. 4.1)). Extinction, c(Hβ), maps, both with and without the scattering component included, were produced from ratioing Hα/Hβ and comparing the projected spaxel value to Case B. The difference of these two images showed the resultant effect of dust scattering on the measured extinction.

Many models were run slightly altering the dimensions of the components in Table C.1, their densities, filling factors and G/D ratios. The dust shells were explored by selectively turning off their scattering and or extinction of the emission. The power law of the AMC grains was also adjusted for lower or higher a_{min} and a_{max} to simulate a smaller or larger MRN mean size. With AMC grains and C_{60}, the wavelength dependence of the scattering properties (viz. grains smaller than the wavelength of light being scattered) naturally led to higher scattered flux at Hβ relative to Hα). But none of the extensions of the dust properties proved capable of producing such a large decrease in apparent extinction in the rim around the Tc 1 bright core, as observed in Fig. 4, maximum 0.07 dex. For example, increasing the density of AMC scattering grains in Dust Shell B did not necessarily lead to larger scattered flux towards the observer, as the extinction along the line from the emission voxel to the scattering voxel reduces the incident radiation on the scattering voxels.

Figure C.1 shows a representative model employing AMC as described in Table C.1. The projected gas and total dust density

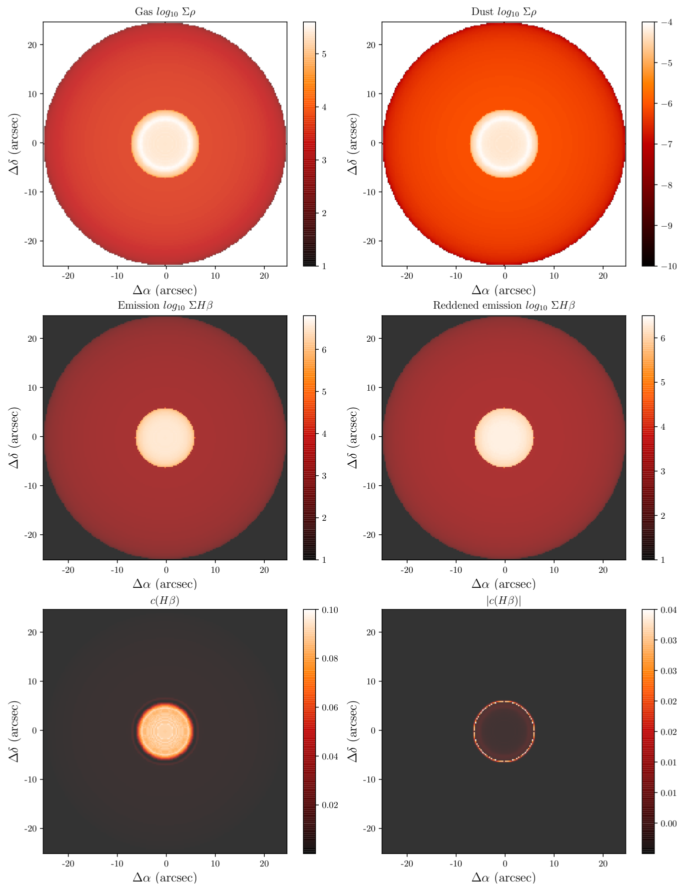

Fig. C.1. Overview of the modelling results for a representative model employing AMC dust only and summarized in Table C.1.
Upper row: the $\log_{10}$ model surface gas density per cm^3 (left) and $\log_{10}$ surface dust density (right), designated by Σ;
Middle row: intrinsic (without line-of-sight extinction) $\log_{10}$ surface density in Hβ emission in erg cm^{-2} s^{-1} × 10^{20} (left) and observed Hβ emission with line-of-sight extinction (right);
Lower row: extinction, c(Hβ), from the model Hα/Hβ ratio images – (left) for the extinction (i.e. sum of dust absorption and scattering), and (right) for the extinction decrement induced by the dust scattering only (expressed as |c(Hβ)|).
Axes show offsets with respect to the position of centre of the model (assumed position of the CSt).

(sum of core, halo and Dust Shells A & B contributions) of this model are shown in the upper panels; the middle panels show a $\log_{10}$ image of intrinsic Hβ emission (i.e. without extinction) and the observed Hβ emission (with extinction by the intra-nebula dust); the lower panels show the image of the extinction, c(Hβ), derived from the ratio of the model Hα and Hβ images compared to Case B and the extinction difference (expressed as |c|) induced by the scattering from dust. While the results give a large-scale approximate match to the observed nebula, many details are lacking. For the extinction images, the mean value of extinction to the core nebula was reproduced ($c \cong 0.07$, after subtracting the interstellar extinction), but the magnitude and morphology of the annulus of extinction deficit was poorly reproduced, with only a narrow rim of peak values, even though the Dust Shell B is broader (Table C.1).

In the case of the scattering by C_{60} molecules, the density was arbitrarily increased to try to reach a reduction in extinction c(Hβ) comparable to the observed value. Such decrements could be achieved but with a shell of very high density ($1.0{\times}10^8$ cm^{-3}, Dust Shell C in Table C.1). For the set of parameters in the table, the density of C_{60} molecules is then 5500 cm^{-3}. This would require a factor $\sim 10^5$ increase in C/H relative to the value for the core nebula determined by Aleman et al. (2019) with a density $\sim$3000cm^{-3}. Even allowing that one AMC grain in the MRN distribution representative of the mean size could break down completely into about 9000 C_{60} molecules (based on ratio of grain masses), such a density of C_{60} molecules is extreme. This result would imply very exceptional conditions in the shell of dust around the Tc 1 core without a signature in the gaseous emission; it is concluded that scattering by fullerene molecules only cannot account for the apparent extinction deficit.

Appendix D: Comparison of residual continuum (dereddened spectrum – nebular continuum) for MUSE observations of NGC 7009, NGC 4361, and Tc 1

Already in Walsh et al. (2018) and Walsh et al. (2024) evidence was presented of an excess continuum above the nebular continuum for NGC 7009 (Fig. A.1) and for NGC 4361 (Fig. 9). Here we compare these excess continua with that for Tc 1, to investigate any similarities in the shape of the residual continuum for the three PNe with MUSE observations and determinations of their nebular continuum.

The residual spectra were calculated from the dereddened spectrum of the total nebular flux collected in the MUSE observations (with the area of the CSt point spread function excluded) – the fitted nebular continuum (bound-free [b-f] and free-free [f-f] for H I, b-f for He I and b-f+f-f for He II and 2-photon for H I and He II). The adopted parameters and physical conditions for the nebular continuum computation are listed Table D.1. The emission lines in the residual spectra were fitted by Gaussians and removed but there were many fainter lines not in the list of fitted lines, as well as residuals of sky subtraction (telluric emission and absorption). These features confused the comparison of the three spectra. The spectra were thus interactively cleaned to remove the traces of emission lines and sky residuals with the aim to arrive at a representation of the continuum. Fig. D.1 shows the cleaned residual continuum for Tc 1, NGC 4361 and NGC 7009. For the brightest lines that displayed broad line wings, the residual profile was cut at some maximum for display purposes. To enable direct comparison, the three spectra have been normalized to the same mean flux at 7000 Å. The region between 8195 and 8440 Å was blanked out in this plot since it was not possible to effectively fit all the closely spaced high Paschen (and in the cases of NGC 4361 and NGC 7009, also the He^{++}, n=5-9 and n=6-36 ... 6-50) lines.

The shapes of the residual spectra showed remarkably close similarity for Tc 1 and NGC 4361, despite their very different extinction and ionization conditions. All three PNe residual spectra exhibited the rise at ≳ 9000 Å caused by the MUSE 2nd order contamination. A power law in λ^{-3} fitted these two residual spectra quite well over the range 4700–8000 Å. For NGC 7009, there was some similarity in the overall shape, but the continuum S/N of this spectrum was lower than those for NGC 4361 and Tc 1 on account of the observational requirement to detecting unsaturated emission lines (exposure is a combination of 4 10 s exposures). The broad wings under the very strong emission lines in NGC 7009 (O III5007 Å was already saturated in this short exposure) complicated the comparison below 5600 Å. The broad pedestal to the strongest lines is interpreted as the grating line profile; for Hα (as a single very strong line), its level is

Table D.1. Parameters of the nebular continuum fits to total spectra of three PNe

Nebula	c(Hβ)	Dered F(Hβ)	T_e H I	T_e He I/II	N_e (cm^{-3})	He$^+$/H$^+$	He^{++}/H$^+$
Tc 1	0.31	4.77×10^{-11}	8550	9150	2410	0.0920	
NGC 4361	0.10	1.85×10^{-11}	7500	17000	1500	0.0041	0.0951
NGC 7009	0.12	1.93×10^{-10}	9600	9600	2500	0.0718	0.007

Notes. Adopted physical parameters used to calculate the nebular continuum for Tc 1, NGC 4361 and NGC 7009; compare to Table 3 for Tc 1. See Walsh et al. (2024) for NGC 4361 and Walsh et al. (2018) for NGC 7009.

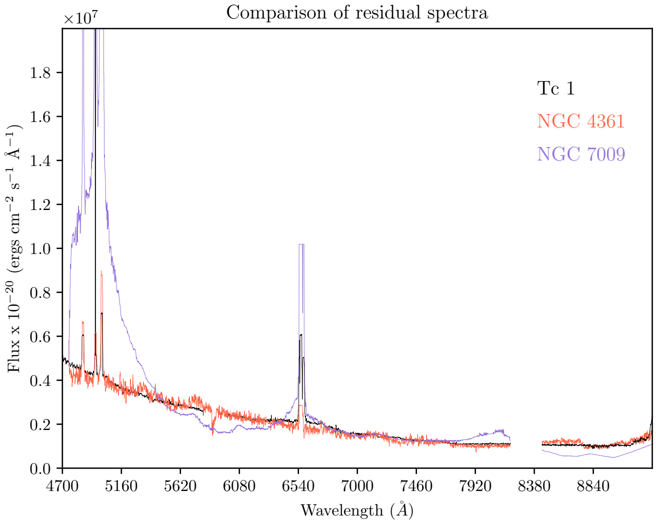

Fig. D.1. Comparison of the residual spectra (i.e. dereddened spectrum of the total nebular flux collected in the MUSE observations – the fitted nebular continuum, as calculated from the parameters in Table D.1), is shown between Tc 1, NGC 4361 (Walsh et al. (2024) and NGC 7009 (Walsh et al. 2018). All spectra have been cleaned of narrow emission lines and sky subtraction residuals and normalized to the same flux at 7000 Å. See text for further details.

~7.7×10^{-5} at 100 Å offset from peak. A weaker pedestal is also visible to Hα in Tc 1[10]. Probably there was a nebular-specific component to these line wings in addition to instrumental effects, since their strengths relative to the line peak differed between Tc 1 and NGC 7009.

Given that the three spectra all have the common presence of a hot star, while the nebular continuum spectra do not, it seems most probable that some small fraction of the flux of the CSt is distributed over the nebula. Although the T_{eff} of the three PNe differ (31 000 K for Tc 1, 85 000 K for NGC 4361 and ~95 000 K for NGC 7009), the optical residual spectra had very similar slopes ($\propto \lambda^{-4}$). However the residual continuum instead follows λ^{-3}, so that some 'reddening' of the CSt continuum is required. A possible mechanism could be internal extinction, but the amount required to change a λ^{-4} slope to λ^{-3} is rather large (c(Hβ) ~ 0.5 dex.). An instrumental origin for this residual continuum still seems more likely, but has difficulties explaining how the extinction-corrected residual continua are so similar. The same residual spectra (dereddened – nebular continuum) for other PNe with differing CSt properties (for example with a strong line-of-sight reddening to the CSt) could offer other possibilities to test the origin of this residual continuum.

[10] This profile is much wider than the ~1000 km s^{-1} FWHM profiles reported on strong lines in Tc 1 by Aleman et al. (2019).

Table E.1. Tc 1 MUSE Region Spectrum: Core

Rest λ (Å)	Line species	Observed flux	Error flux	Dered flux	Error flux
4713.1	He I	0.500	0.002	0.514	0.017
4754.8	[Fe III]	0.115	0.001	0.118	0.004
4861.2	H4	100.000	0.000	100.000	0.000
4880.9	[Fe III]	0.116	0.001	0.116	0.004
4921.9	He I	1.253	0.002	1.239	0.040
4958.8	[O III]	15.417	0.006	15.147	0.487
4987.4	[Fe III]	0.063	0.001	0.062	0.002
5006.8	[O III]	46.535	0.012	45.327	1.450
5015.5	He I	2.733	0.002	2.658	0.085
5040.9	Si II	0.083	0.001	0.080	0.003

Notes. Relative fluxes with respect to flux Hβ = 100.0;
Observed Hβ normalizing flux: 5.67 ×10^{-12} ± 4.85×10^{-16} erg cm^{-2} s^{-1};
Dereddened Hβ normalizing flux: 1.19 ×10^{-11} ± 1.36×10^{-13} erg cm^{-2} s^{-1};
Extinction c = 0.320 ± 0.005 calculated with T_e = 9000 K; N_e = 2200 cm^{-3}.
Only the first ten entries of this table are shown; the full table is available in electronic form at the CDS.

Appendix E: Spectra of the Tc 1 integrated regions – Core, low c, halo, and total nebula

Lists of line identifications and Gaussian fluxes for the spectra of the three annular regions and the total spectrum of the full nebula (excluding an area around the CSt) are presented. See Sect. 5.4 for details on the extent of the integrated regions. Line identifications are taken from the line flux lists in Aleman et al. (2019), Appendix A. The line flux errors were propagated from the flux error per pixel, provided by the MUSE data reduction pipeline, through the Gaussian fitting via the covariance matrix. The flux errors for the dereddened lines include the propagated contribution of the extinction error.

Table E.2. Tc 1 MUSE Region Spectrum: Low c

Rest λ (Å)	Line species	Observed flux	Error flux	Dered flux	Error flux
4713.1	He I	0.402	0.008	0.409	0.028
4754.7	[Fe III]	0.273	0.008	0.276	0.020
4861.2	H4	100.000	0.000	100.000	0.000
4881.0	[Fe III]	0.306	0.006	0.306	0.021
4921.9	He I	1.021	0.007	1.015	0.066
4958.8	[O III]	10.574	0.015	10.470	0.674
4987.4	[Fe III]	0.366	0.006	0.362	0.024
5006.8	[O III]	31.808	0.026	31.341	2.005
5015.5	He I	2.557	0.009	2.518	0.161
5047.5	He I	0.283	0.004	0.278	0.018

Notes. Relative fluxes with respect to Hβ = 100.0;
Observed Hβ normalizing flux: 5.49 $\times 10^{-13}$ ± 1.16$\times 10^{-16}$ erg cm^{-2} s^{-1}
Dereddened Hβ normalizing flux: 8.30 $\times 10^{-13}$ ± 1.91$\times 10^{-14}$ erg cm^{-2} s^{-1}
Extinction c = 0.18 ± 0.01 calculated with T_e = 9000 K; N_e = 1500 cm^{-3}.
Only the first ten entries of this table are shown; the full table is available in electronic form at the CDS.

Table E.3. Tc 1 MUSE Region Spectrum: Halo

Rest λ (Å)	Line species	Observed flux	Error flux	Dered flux	Error flux
4713.6	He I	0.177	0.041	0.181	0.043
4754.1	[Fe III]	0.479	0.046	0.486	0.056
4780.4	N II	0.251	0.041	0.253	0.044
4789.9	N II	0.224	0.005	0.227	0.016
4861.2	H4	100.000	0.000	100.000	0.000
4880.8	[Fe III]	0.457	0.051	0.456	0.059
4922.0	He I	0.400	0.023	0.397	0.034
4958.9	[O III]	12.843	0.055	12.674	0.817
4987.4	[Fe III]	1.716	0.046	1.688	0.117
5006.8	[O III]	38.773	0.076	38.015	2.433

Notes. Relative fluxes with respect to Hβ = 100.0;
Observed Hβ normalizing flux: 1.52 $\times 10^{-13}$ ± 7.27$\times 10^{-17}$ erg cm^{-2} s^{-1}
Dereddened Hβ normalizing flux: 2.63 $\times 10^{-13}$ ± 6.07$\times 10^{-15}$ erg cm^{-2} s^{-1}
Extinction c = 0.24 ± 0.01 calculated with T_e = 9000 K; N_e = 700 cm^{-3}.
Only the first ten entries of this table are shown; the full table is available in electronic form at the CDS.

Table E.4. Tc 1 MUSE Region Spectrum: Total

Rest λ (Å)	Line species	Observed flux	Error flux	Dered flux	Error flux
4713.1	He I	0.483	0.002	0.496	0.033
4754.7	[Fe III]	0.114	0.001	0.116	0.008
4861.2	H4	100.000	0.000	100.000	0.000
4880.9	[Fe III]	0.118	0.001	0.118	0.008
4921.9	He I	1.191	0.001	1.179	0.076
4958.8	[O III]	28.619	0.005	28.133	1.810
4987.4	[Fe III]	0.103	0.001	0.101	0.007
5006.8	[O III]	86.465	0.012	84.289	5.392
5015.5	He I	2.724	0.002	2.652	0.169
5035.5	O II	0.051	0.001	0.049	0.003

Notes. Relative fluxes with respect to Hβ = 100.0;
Observed Hβ normalizing flux: 2.15 $\times 10^{-11}$ ± 9.74$\times 10^{-16}$ erg cm^{-2} s^{-1}
Dereddened Hβ normalizing flux: 4.39 $\times 10^{-11}$ ± 1.01$\times 10^{-12}$ erg cm^{-2} s^{-1}
Extinction c = 0.31 ± 0.01 calculated with T_e = 9000 K; N_e = 1500 cm^{-3}.
Only the first ten entries of this table are shown; the full table is available in electronic form at the CDS.